Volumetric Analysis of Fish Swimming Hydrodynamics using Synthetic Aperture Particle Image Velocimetry

by

Leah Rose Mendelson

B.S., Mechanical Engineering
Franklin W. Olin College of Engineering (2011)

Submitted to the Department of Mechanical Engineering
in partial fulfillment of the requirements for the degree of

Master of Science in Mechanical Engineering

at the

MASSACHUSETTS INSTITUTE OF TECHNOLOGY

September 2013

Author .....
Department of Mechanical Engineering
August 9, 2013

Certified by .....
Alexandra H. Techet
Associate Professor of Mechanical and Ocean Engineering
Thesis Supervisor

Accepted by .....
David E. Hardt
Chairman, Department Committee on Graduate Theses

Volumetric Analysis of Fish Swimming Hydrodynamics using Synthetic Aperture Particle Image Velocimetry

by

Leah Rose Mendelson

Submitted to the Department of Mechanical Engineering
on August 9, 2013, in partial fulfillment of the
requirements for the degree of
Master of Science in Mechanical Engineering

Abstract

This thesis details the implementation of a three-dimensional PIV system to study the hydrodynamics of freely swimming Giant Danio (*Danio aequipinnatus*). Volumetric particle fields are reconstructed using synthetic aperture refocusing. The experiment is designed with minimal constraints on animal behavior to ensure that natural swimming occurs. Resultantly, the fish exhibits a variety of forward swimming and turning behaviors at speeds between 1.0-1.5 bodylengths/second. During these maneuvers, the imaging system is also used to track and reconstruct the fish body. The resultant velocity fields are used to characterize the size and shape of the vortex rings shed by the fish during forward swimming and turning. Results show clearly isolated and linked vortex rings in the wake structure, as well as the thrust jet coming off of a visual hull reconstruction of the fish body. Depending on the maneuver, the amount of symmetry in the wake varies, emphasizing the shortcomings of a single planar slice to characterize these behaviors. The additional information provided by volumetric measurement is also used to analyze the momentum in the fish's wake. The circulation of the vortex rings is computed across several slices of the ring taken through its center axis and analyzed over time. Circulation can be used to compute the fluid impulse in the vortex ring to better understand propulsive performance. The measured impulse, combined with visualization of the wake, provides a comparison between forward swimming and turning based on volumetric measurements. The development of this system lays a foundation for further volumetric studies of swimming hydrodynamics.

Thesis Supervisor: Alexandra H. Techet
Title: Associate Professor of Mechanical and Ocean Engineering

Acknowledgments

I want to first thank my advisor, Professor Alexandra H. Techet, for giving me the freedom to pursue this project and providing substantial guidance along the way. I am grateful for her enthusiasm, practical advice on how to run successful experiments, and insights into deeper analysis of my data. Thanks also for all the opportunities to travel for conferences and fieldwork.

Much appreciation also goes out to my labmates, Barry Scharfman and Abhishek Bajpayee, for all their advice and camaraderie. I am also indebted to my UROP student Juliana Wu for feeding the fish and all the help running experiments, especially all the Friday afternoons of patiently waiting when the fish refused to do anything interesting on camera. I also want to thank all my former and almost labmates for helping me find my way at MIT.

I want to thank my parents, Mark and Terri Mendelson, for their tremendous support, endless encouragement, excellent taste in music, and deep concern for the health of my fish. Thanks also to my brother Jake, whose growth as an engineer and service to the Navy keeps me grounded and broadens the scope of my ideas. Who could have thought we would go from goofy kids on the swim team to where we are today?

I would not have made it this far without the support of my grad student family. Thanks for making this place feel like home. I am also grateful to all the coffee hour regulars for everything I have learned about life and research over bagels early on Friday morning.

I especially need to thank Jacob Izraelevitz, who was always there for me, listened to my research rants, and made sure I kept life balanced and fun.

Lastly, I would like to thank my fish. Sometimes they actually did what I wanted for long enough to take usable data.

Contents

List of Figures

List of Tables

Chapter 1

Introduction

1.1 Context

As nature's quintessential swimmers, fish exhibit a clear and classic relationship between form and function. Fish bodies have evolved to confront diverse survival challenges, and in many applications are unmatched in effectiveness by human invention. As a result, fish swimming has been widely studied to understand its evolutionary origins and to use these behaviors as a source of inspiration for engineering design. However, as with any biological example, the features at play in fish locomotion are complex, and aspects of the fish's physiology may be tied to goals other than efficient movement. Given the complexity of the fish body, experiments on live swimming fish are often necessary to characterize completely the hydrodynamic interactions at hand and identify features with the most locomotive benefit.

Particle Image Velocimetry (PIV) is a commonly-used technique for instantaneous, non-invasive measurement of an entire velocity field with many applications, including visualization of the flow field surrounding a swimming fish. The flow is seeded with tracer particles, which are illuminated using a planar sheet of laser light. The location of the particles over time is filmed using a digital camera. Each particle image is then broken into windows, which are cross-correlated between successive frames to determine the velocity in each window [35]. A summary of PIV methodology and history is presented by Adrian [3].

PIV conventionally provides information about a 2D slice of the flow field. However, the fish body is clearly three-dimensional and many of the most interesting swimming behaviors are far from planar in nature. Fish are known in particular for their maneuverability and ability to execute turning and jumping behaviors faster, more efficiently, and in smaller spaces than manmade ocean vehicles. Several species exhibit unique maneuvering behaviors with the potential to solve especially significant engineering challenges (fig. 1-1). For instance, archer fish sight their prey from a stationary position below the surface and then execute a powerful, accurate jump to reach their target. Furthermore, bluefin tuna are able to swim at high burst speeds while maintaining their propulsive efficiency. Flying fish are able to hover and glide above the water's surface as a result of large, winglike fins. These behaviors are both

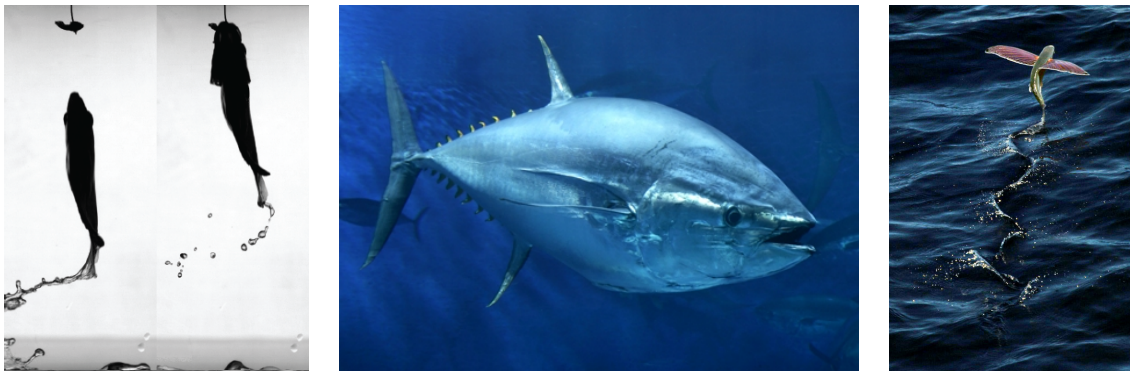

(a) Archer fish jumping [60] (b) Bluefin tuna maneuvering (c) Flying fish hovering

Figure 1-1: Examples of unsteady three-dimensional swimming behaviors. Tuna photo from the *Tuna Research and Conservation Center* (www.tunaresearch.org). Flying fish photo from *National Oceanic and Atmospheric Administration* via Wikimedia Commons.

unsteady and highly three-dimensional; it is not ideal to constrain such complex maneuvers to a single plane for analysis. In addition, study of these scenarios requires substantial spatial and temporal resolution. As a result, conventional planar 2D PIV techniques will not provide a complete picture of the hydrodynamic interactions at play. Instead, volumetric PIV techniques are necessary to analyze these flows.

Three-dimensionality has proven non-trivial in a number of swimming applications, and numerous studies have acknowledged the limitations of using planar mea-

surements to study swimming hydrodynamics [68, 69]. Furthermore, in a review of the current state of fish hydrodynamics research, Lauder cites three-dimensional interactions as some of the most critical aspects of swimming analysis for engineers and biologists to consider as instrumentation develops to understand these behaviors [39]. Three-dimensional considerations must also be extended to the development of biomimetic robots and vehicles [41], particularly in determining the importance of secondary fins and propulsors that would complicate the design and production of such vehicles. One example of a bio-inspired vessel uses the hull shape and kinematics of a tuna as the foundation of an underwater autonomous vehicle for ocean surveillance. Likewise, a robotic flying fish could be used to take measurements below and above the ocean surface (fig. 1-2).

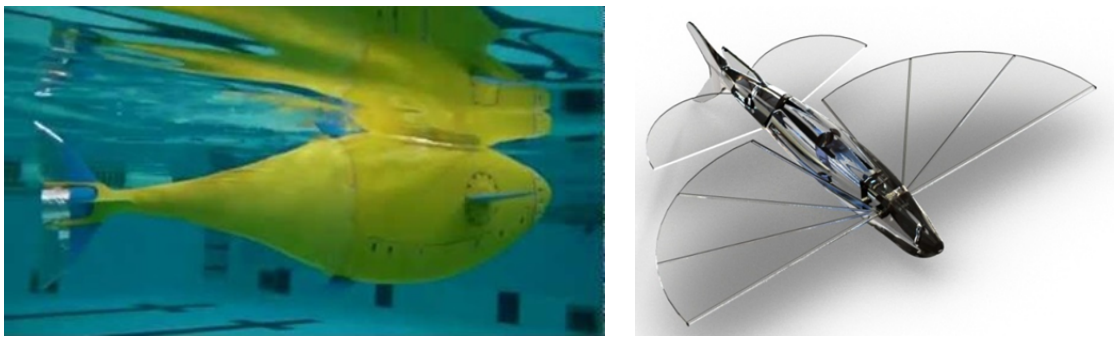

(a) Robotic tuna fish [10]

(b) Robotic flying fish [24]

Figure 1-2: Biomimetic robots based on the unique propulsive behavior of the tuna and air/sea versatility of the flying fish.

Substantial scholarly attention in recent years has focused on methods of expanding PIV capabilities to three dimensions, with numerous techniques developed for this purpose. Specifically, synthetic aperture PIV (SAPIV), a 3D PIV technique based on light field imaging principles developed within the computer vision community [9], shows particular potential in biomimetic applications. This method provides a large number of viewpoints to see around a body in the flow field. SAPIV also utilizes computationally simple reconstruction algorithms for efficient but accurate processing. This capability is crucial for effectively working with large sets of high-speed time-resolved volumetric data such as those generated in the study of unsteady

applications.

1.2 Outline of Thesis

This thesis details the design and implementation of a synthetic aperture PIV system for the study of fish locomotion. This work also introduces additional methods of hydrodynamic analysis made possible through the volumetric data that 3D PIV provides.

Chapter 2 provides necessary background information on the fluid physics of fish locomotion and previous image-based experimental analysis of swimming behaviors. The review focuses especially on work performed in unsteady maneuvering scenarios. This section also details several 3D PIV methodologies, their working fundamentals, and the limitations of these methods. Particular attention is paid to previous applications of these techniques to swimming hydrodynamics.

Chapter 3 introduces in detail the principles of synthetic aperture PIV and the use of this specific PIV technique to study to swimming hydrodynamics. This section outlines the computational steps to reconstruct particle fields using light field imaging and synthetic aperture refocusing. The practical aspects of running 3D PIV experiments, especially coupled with working with live animals, are also discussed in detail. Finally, this chapter introduces a method to track and reconstruct the fish body in the measurement volume.

Chapter 4 examines how the results of these SAPIV experiments can be used for quantitative analysis of the momentum transfer between the fish and the fluid during swimming behaviors. In particular, methods will be presented for analyzing the size and geometry of wake features. This information is then used in the calculation of circulation and fluid impulse in the wake. Volumetric data is also used to evaluate the reliability of planar experiments to determine the same quantities.

Chapter 5 summarizes the contributions of this work and proposes several directions for further research. These avenues of research are based on improvements to the underlying imaging techniques, expanded data analysis methods for volumetric

measurements, and applications to specific biomimetic behaviors ripe for 3D analysis.

Chapter 2

Background

2.1 Fish Locomotion

Fish locomotion has long fascinated scientists, mathematicians, and engineers across disciplines. Analysis of these swimming behaviors relies on a combination of experiments, both on live fish and mechanical simplifications such as flapping hydrofoils, simulations, and analytic models. Image-based analysis is the backbone of experimental research on swimming hydrodynamics and provides the observations on which theory and models are built. Advances in imaging technology are closely followed by increased knowledge of swimming hydrodynamics obtained by implementing these new developments. Imaging studies have been used to characterize the kinematics of swimming gaits, as well as the wake structures left behind by these behaviors. Through particle image velocimetry, digital imaging techniques have served as the basis for thorough quantitative analysis of wake structures and near-body flow around the fish.

Kinematics Early studies on fish locomotion placed heavy emphasis on the kinematics of the swimming gait exhibited by the fish. In the first section of Gray's seminal "Studies in Animal Locomotion" articles, the author reports wave patterns in the eel versus those of several species of fish based on photographs of each organism's swimming silhouette [27]. Based on similar kinematic observations, Sir James

Lighthill developed his fundamental analytic theory for oscillatory swimming behaviors [44]. However, Lighthill acknowledges shortcomings to his two-dimensional model based on the three-dimensional physiology of the fish body. Specifically, Lighthill cites three-dimensionality as the motivation for the convergent evolution of lunate tails in fast-swimming fish. According to his theory, in 2D a straight trailing edge would be optimal, thus the tail shape must have some added 3D benefit [44]. More recent kinematic studies have taken advantage of high-speed imaging to characterize body-line motions during unsteady swimming at high temporal resolution. For instance, Domenici and Blake describe the high-speed kinematics of burst swimming during fast-starting behaviors [14].

Wake visualization While the fish body silhouette is easy to film, specialized visualization techniques are needed to understand the link between swimming kinematics and the wake structures they created. Early qualitative visualizations were performed by Rosen [54], who swam a pearl danio (*Brachydanio albolineatus*) through a layer of milk and recorded the wake patterns of the fish. Similarly, McCutchen used shadowgraphy to image a fish swimming in water of varied temperature and thus refractive index. These images visually confirmed a series of vortex rings in the wake generated during steady and "push and coast" swimming modes [47]. McCuthchen's visualizations were sufficient to calculate the overall speed of the body and the Froude efficiency of propulsion during steady and unsteady swimming modes, but failed to resolve full velocity distributions in the flow. Beyond the qualitative nature of these techniques, another critical limitation is animal welfare; the fish cannot be disturbed by the visualization method if it is to produce accurate hydrodynamic results.

Hydrodynamic Forces Efforts have been made to analyze the energetic cost of swimming by combining kinematic data with measurements of oxygen consumption, metabolic rates, and the physical properties of fish muscle fibers [73]. However, complete characterization of the momentum transfer during swimming requires high-speed kinematic analysis of the fish (to characterize the change in momentum of the body),

coupled with high-spatial resolution analysis of the wake (to measure the momentum transferred to the fluid). Particle image velocimetry (PIV) can be combined with kinematic analysis to provide information about the wake and trajectory of the fish with the resolution necessary for thorough hydrodynamic force analysis.

2.1.1 PIV Experiments on Swimming Fish

Planar PIV has played an instrumental role in analyzing biological flows. Early applications of 2D PIV to fish by Wolfgang et al. [74], Stamhuis and Videler [63], and Müller et al. [49] confirmed that their wake viewed in a single plane is a reverse Kármán street, as predicted by earlier visualizations and theory. Results clearly showed staggered vortices of alternating sign with a center axial thrust jet always moving in the direction away from the body. The vortex pairs seen in the street are slices through the rings suggested by McCutchen's visualizations. Drucker and Lauder extended similar results taken in multiple body planes to a series of staggered vortex rings in 3D, and demonstrated linking of the vortex cores between subsequent rings at high swimming speeds [15]. In similar wake studies on unsteady swimming, high-speed imaging holds particular benefit providing the time resolution required to address instantaneous behaviors [40]. For instance, high-speed implementations of PIV have been used to characterize the flows generated by fast-starting Giant Danio [18], bluegill sunfish pectoral fins [40], and numerous man-made simplifications (e.g. [16]).

2.1.2 Hydrodynamic Analysis from PIV Data

For biomimetic engineering design, such as vehicles developed by Barrett et al. [7], Fish et al. [20], and Epps et al. [19], visualization of the flow field must be accompanied by quantitative measures of hydrodynamic forces and impulse during swimming behaviors. The fluid impulse is one measure of the momentum in a vortex. Impulse

for a general vortex filament is given by

$$I = \frac{1}{2}\rho \int_V \mathbf{x} \times \omega dV, \tag{2.1}$$

where ρ is the fluid density, ω is the vorticity, and V is the volume of the vortex. Vorticity is a vector measure of the spinning motion of a fluid and is determined from the velocity field as

$$\omega = \nabla \times u. \tag{2.2}$$

In a planar slice through the vortex, vorticity can be related to the circulation Γ of a vortex by

$$\Gamma = \int_A \omega \cdot n dA, \tag{2.3}$$

where n is the unit normal vector of the slice and A is the area of the vortex in the slice plane. As a result, in the case of an axisymmetric vortex ring, impulse can be determined from the circulation and vortex ring diameter as

$$I = \rho\Gamma\frac{\pi D^2}{4}, \tag{2.4}$$

where D is the vortex ring diameter. In this thesis, the circulation Γ will be calculated from velocity data as

$$\Gamma = \oint_C u \cdot dl, \tag{2.5}$$

using the line integral of tangential velocity on a closed contour around the vortex to minimize error in calculation. Applying Stokes' theorem and integrating vorticity over area first requires calculation of vorticity, thus introducing more uncertainty into the calculation than working with velocity data directly.

The total impulse in the wake is a measure of the momentum transferred from the fish to the water and must balance with the change in momentum of the fish body during the maneuver [49, 18]. During acceleration, the change in momentum of the fish is given by

$$I = (m + m_{11})\Delta V, \tag{2.6}$$

where m is the mass of the fish, m_{11} is the added mass of the fluid surrounding the fish, and ΔV is the change in velocity of the fish during the maneuver.

This framework is the simplest model of the wake possible for analysis and used as a benchmark for the calculation of hydrodynamic impulse from volumetric PIV data. Work by Epps and Techet [18] introduces other contributions to the fluid impulse model that must be considered for a complete characterization of the wake vortex dynamics. Dabiri presents an alternate method of momentum analysis that determines unsteady forces instead of impulse by considering the added mass of the wake vortex [11].

In planar PIV studies, three-dimensionality contributes to disagreement between wake and fish impulse. Impulse is related to the overall vortex filament shape, which is not always a perfect ring. Furthermore, experiments are unable to image vorticity forming at points in the body outside the measurement plane, such as the fish's nose in Epps and Techet [18]. Volumetric data is capable of characterizing and overcoming these limitations. 3D data provides infinite measurement planes for 2D impulse computation, thus the uncertainty bounds of a single planar slice can be determined. Volume measurements also provide more details on the geometry of each vortex shed by the fish and the relationship between multiple patches of vorticity in the measurement region.

2.2 3D PIV

Three-dimensional PIV measurements can be obtained using a number of imaging and reconstruction techniques. Several of these methods are described by Kitzhofer et al. [37]. However, 3D PIV is still a developing field, and each method has its own experimental constraints, advantages, and limitations. Current hurdles in the application of these techniques include limits on seeding density, aspect ratio (the resolvable depth in the third dimension is often much less than the other two dimen-

sions), and spatial resolution. 3D PIV is also predominately used as a visualization tool, and most application work to date is qualitative. However, in this work, it is necessary to utilize a technique that yields sufficient data for quantitative impulse analysis. A review of 3D PIV methods is necessary to understand their roles in the study of 3D swimming behaviors, and also the selection of synthetic aperture PIV for the current study.

In this summary and the remainder of the thesis, the X-Y plane refers to the plane of a single 2D PIV image, while Z is the out-of-plane, additional dimension needed to make a volumetric measurement.

2.2.1 Review of 3D PIV Methodologies

Stereoscopic PIV In conventional 2D PIV, processing does not consider small amounts out-of-plane motion within the light sheet; motion in the Z-direction is projected onto the X and Y velocities determined by the cross-correlation. Stereoscopic PIV (stereo-PIV) eliminates this problem by using two viewpoints to resolve the depth of particles within a thin light sheet. Several imaging configurations and reconstruction techniques exist for stereo-PIV [53], but the common thread is that depth reconstruction within the illuminated sheet can be used to provide the third velocity component. As a result, stereo-PIV can be used to evaluate the three-dimensionality of a flow and the relative importance of in-plane and out-of-plane motion. However, since the measurement region is still a single X-Y plane, stereo-PIV falls short of a complete volumetric characterization of the flow field.

Holographic PIV Holographic PIV is a volumetric PIV technique that determines the depth of a particle from the interference pattern of light scattered by the particle compared to a reference light source [31]. The recording medium is typically a photographic plate placed behind the measurement volume. Unlike the typical CCD camera, which has a finite pixel size determined by the camera sensor and a limited depth of field governed by the lens numerical aperture ($f\#$), holographic recording has much higher spatial resolution and limitless depth of field. However, the plate

used for holography requires specialized film and developing processes before any data can be processed. Methods for digital holographic PIV reduce the material difficulties of the setup, but are limited in the size of the measurement volume and seeding density [48].

Defocusing Digital PIV Defocusing Digital PIV (DDPIV) exploits coded particle blur to determine the depth of a particle [52]. All particles are imaged through a specialized aperture, such as a triangular pattern of pinholes, and the spacing of the pattern on the image corresponds to distance in the Z-dimension. The pattern between the particle images on each camera sensor must be clear to reconstruct the depth, giving the technique limited effectiveness at higher seeding densities where clear constellations cannot be determined.

Tomographic PIV Tomographic PIV, first introduced by Elsinga et al. [17], takes a multi-camera approach to 3D intensity field reconstruction. This method uses the principles of optical tomography to reconstruct particle fields, and is described in detail by Scarano [56]. Tomo-PIV experiments typically use between 4-8 cameras around a measurement volume, with each camera fitted with a high numerical aperture lens for sufficient depth of field and a Scheimpflug adapter to align the plane of camera focus with the measurement volume. Measurement volumes for tomo-PIV are typically generated by expanding a light sheet to a quarter of the X-Y field of view. Particle volume reconstruction is performed using iterative algorithms, including many variations of the Multiplicative Algebraic Reconstruction Technique (MART) [5, 51, 13]. Since many passes of these algorithms are necessary for accurate results, reconstruction requires substantial computational power and processing time, sometimes over a day for a single high-resolution particle field on an eight core computer [28]. Substantial current research attention is directed to further development of the tomo-PIV technique and its applications, particularly the three-dimensional characterization of turbulence [56].

Plenoptic PIV Three-dimensional reconstruction can also be performed through light field imaging techniques. In computational photography, the light field is the amount of light passing in every direction at every location in a volume. A 2D image can only generate a slice of the light field, thus multiple samples of the light field are needed to fill up the volume. Plenoptic imaging generates multiple images of the light field by using a lenslet array to segment incoming light into several images on a high-resolution CCD camera. The particle reconstruction from a plenoptic (light field) camera can then be used to perform PIV [46, 66]. Since the entire light field is recorded with a single, high-resolution CCD image sensor, the frame rate of plenoptic cameras is typically much lower than individual cameras working in parallel. For instance, plenoptic cameras produced by Raytrix [26] typically can reach frame rates of 10 Hz at 3 megapixels (Raytrix R11) or 5 Hz at 7.25 megapixels (Raytrix R29), far slower than is necessary for time-resolved measurements.

Synthetic Aperture PIV Light field imaging can also be performed using an array of cameras. Synthetic aperture PIV is a multi-camera method similar to tomo-PIV, but the SAPIV technique relies on light field imaging algorithms for reconstruction instead of tomography. The working principles of SAPIV will be described in detail in Chapter 3. Simulations have shown the possibility of analyzing cubic measurement volumes at reasonably high seeding densities and computational time far less than that using tomo-PIV algorithms [9]. Synthetic aperture imaging can also reconstruct objects in partially occluded volumes, an advantage for working with a body in the flow. As a new 3D PIV technique, significant development and application work is necessary to determine the feasibility of this method as a tomo-PIV alternative. One goal of the current study is to evaluate the feasibility of SAPIV experiments in an application where there is a significant need for three-dimensional measurements and a unique set of experimental challenges (working with a living, arbitrarily-moving specimen).

2.2.2 3D Measurements of Fish Swimming

Several studies have previously attempted to characterize fish wake dynamics in full three-dimensional forms using the aforementioned techniques. Using stereoscopic PIV, Sakakibara et al. resolved substantial out-of-plane velocity during rapid fish turning [55] and proved the need to consider three-dimensionality in maneuvering applications. The first volumetric PIV on fish, taken using defocusing digital PIV (DDPIV) by Flammang et al. [22], provided complete visualization of three-dimensional vortex rings coming off the caudal fins of bluegill sunfish and cichlid fish swimming in a flume. Results also showed smaller vortices generated by the dorsal and anal fins. The behavior of these features emphasized the need to consider interactions between secondary fin vortices and the caudal fin wake in a volume instead of a plane. Using the same 3D PIV technique on the caudal fin wake of a dogfish shark, Flammang et al. observed a novel dual-linked vortex ring structure far more complex than a 2D slice through this feature would suggest [21]. These findings further accentuate that biological flow structures are more complex than how they are modeled in 2D. 3D PIV has also enabled the study of behaviors that cannot be simplified to a single plane for analysis such as Adhikari and Longmire's use of tomographic PIV to study predator-prey dynamics in zebrafish feeding [2]. This study also introduced a visual hull method for object reconstruction and masking that enables 3D PIV to be applied to near-body flows as well as wake features.

Accurate analysis of swimming hydrodynamics requires natural behavior from the fish being studied. As a result, disturbances to the fish during experiment execution must be minimized as discussed by Stamhuis et al. [64]. In particular, the green wavelengths of laser light (λ = 527-532 nm) typically used during PIV in water can disturb fish and provoke unnatural swimming behavior. Near-infrared illumination (λ = 808-810 nm) is invisible to fish and eliminates this problem. Near-IR has been used to visualize unsteady fish maneuvering [18], feeding [2], and plankton flow [50] without the awareness of the organism being studied. Fish are also known to adjust their kinematics in response to the flow field surrounding them, as seen by Liao et al. when

observing swimming gaits behind a cylinder wake [43]. Volumetric measurements can also provide more detailed information about the ambient flow surrounding the fish and identify features outside of a single measurement plane that might impact swimming behavior.

Chapter 3

Application of Synthetic Aperture PIV to Swimming Hydrodynamics

3.1 Synthetic Aperture PIV

Synthetic aperture PIV (SAPIV) reconstructs 3D particle fields using light field imaging algorithms to combine particle images taken using an array of cameras [9]. General principles of light field imaging with large camera arrays are discussed by Isaken et al. [32], Vaish et al. [71], and Levoy [42]. By imaging a scene with multiple cameras, each with a different line of sight, images can populate information about an entire 3D light field instead of a 2D slice of the volume. Synthetic aperture refocusing simulates the effects of a camera with a narrow depth of field scanning through the light field. By spatially relating all the cameras to a global coordinate system (divided into focal planes throughout the measurement volume), combining images, and determining where features are in focus, the 3D location of a particle can be determined. (fig. 3-1).

Refocusing is performed using a modified version of the additive map-shift-average algorithm introduced by Belden et al. [9]. Cameras are first mapped to a reference global coordinate system using a homography transformation [30]. Next, raw images from all cameras at one timestep are shifted to match the projected coordinates of each focal plane within the volume. Finally images from all cameras are averaged to

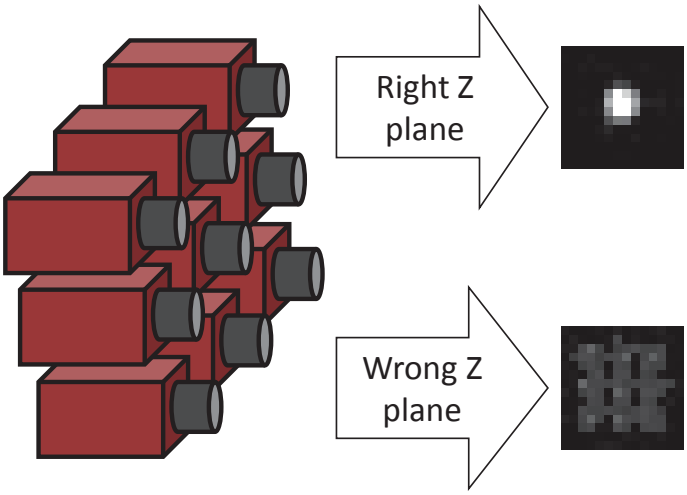

Figure 3-1: Principle of particle localization for SAPIV. Particles from all raw images map to a bright coherent particle at their actual depth, and to fainter, incoherent noise in other planes.

obtain the refocused image at each depth.

3.1.1 Camera Calibration and Mapping

Since imaging is performed through two refractive interfaces, the glass tank wall and the water, the camera array is calibrated using an optimization procedure that compensates for refractive effects [8]. A flowchart of the calibration routine is presented in fig. 3-2.

First, point correspondences between global and image coordinates are determined by traversing a chessboard grid of known size (for this study a 5 mm grid was used) along the Z-axis through the entire measurement volume. The Z-position of the grid in each image is noted for use initializing the solver. A sample calibration image can be seen in fig. 3-3. Each internal corner in the grid is detected in image coordinates using a corner finder algorithm from the RADOCC toolbox [34].

The calibration solver uses the user-provided initial Z-position of the grid and the grid spacing to determine an initial guess for the camera parameters (position, rotation, and magnification) using a pinhole camera model. The pinhole model neglects any lens or refractive effects and is described in detail by Hartley and Zisserman [30].

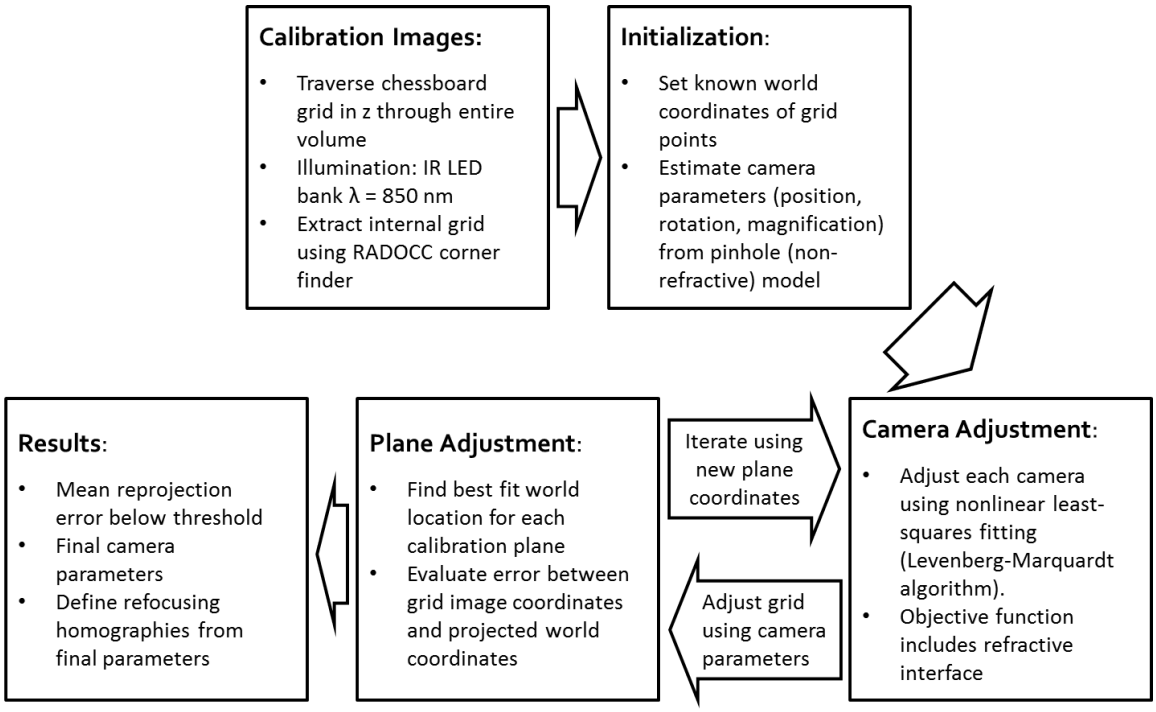

Figure 3-2: Flowchart of the camera array calibration procedure for SAPIV in refractive media.

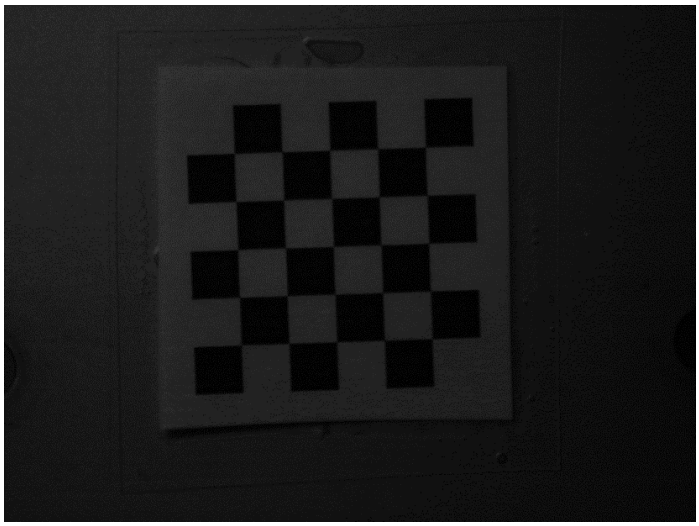

Figure 3-3: Sample calibration chessboard image for the camera array.

The parameters for each individual camera are then adjusted to optimize the mapping of the image coordinates to world coordinates using a nonlinear least-squares solver (Levenberg-Marquardt algorithm). The objective function for this solver includes both refractive ray-tracing from the location in the tank to the outside of the tank

walls and the camera projection from the outside of the tank walls to the image. Next the best fit of all the extracted points onto a physical plane across all the cameras is determined, following which the cameras are adjusted individually again with the new coordinates. Adjustment of the cameras and the grid iterates until the mean reprojection error, the deviation in pixels between the initial measured corners and the pixel locations of the corresponding world points when projected through each camera, is below a specified tolerance. The final camera parameters are then used to define both a projective matrix for each camera and transforms at each desired focal plane.

The mean reprojection error is used as a metric for the optimization, but this measure should not be mistaken for the amount of error in particle reconstruction. The grid used for itself can introduce deviations between world and image coordinates from its printed resolution, mounting the grid perfectly planar within the tank, or a small amount of distortion from laminating the grid for waterproofing purposes. The mean reprojection error for the current study is 0.52 pixels. As a lower bound on the error metric, the mean reprojection error for synthetic calibration data with the same dimensions generated using Blender rendering software [23] is 0.06 pixels. The mean reprojection error when the Z-coordinates of the calibration plate were initialized in the reverse orientation (front image to the back and back image to the front), causing the solver to converge to blatantly nonphysical values, is about 4 pixels, almost an order of magnitude higher than the actual locations and two orders higher than in simulation.

3.1.2 Refocusing

Following this calibration routine, the coordinate frame for refocusing is aligned with the tank, with the X-Y plane parallel to the long axis of the tank and the Z-axis perpendicular to the front wall. The calibration results are used to define homography transforms to relate raw images from each camera to a global frame:

$$\begin{pmatrix} bx' \\ by' \\ b \end{pmatrix}_i = \begin{bmatrix} h_{11} & h_{12} & h_{13} \\ h_{21} & h_{22} & h_{23} \\ h_{31} & h_{32} & h_{33} \end{bmatrix}_i \begin{pmatrix} x \\ y \\ 1 \end{pmatrix}_i \tag{3.1}$$

In this transformation, the h matrix consists of the homography components, x and y are the raw image coordinates, x' and y' are the reference image coordinates, b is a scale factor, and i is the index of a particular camera.

Next, raw images from each timestep are shifted to match the projected image coordinates of features at a specific depth in the volume using another transform:

$$\begin{pmatrix} x'' \\ y'' \\ 1 \end{pmatrix}_i = \begin{bmatrix} 1 & 0 & \mu_k \Delta X_{c_i} \\ 0 & 1 & \mu_k \Delta X_{c_i} \\ 0 & 0 & 1 \end{bmatrix}_i \begin{pmatrix} x' \\ y' \\ 1 \end{pmatrix}_i \tag{3.2}$$

For this mapping, x" and y" are the refocused coordinates at a given depth k, μ_k is a scale factor for that depth, and ΔX_{c_i} is a shift factor to align all camera centers.

All of the images for a given focal plane are finally averaged as

$$I_{SA_k} = \frac{1}{N} \sum_{i=1}^{N} I_{FP_{ki}} \tag{3.3}$$

where I_{SA_k} is the refocused image at a given focal plane, N is the number of cameras, and $I_{FP_{ki}}$ is the transformed image from each camera on that focal plane. The resolution of a SAPIV system was shown by Belden et al. [9], to be a function of the camera optics and the baseline spacing parameter, $D = \frac{\Delta X_c}{s_0}$, where ΔX_c is the distance between camera centers and s_0 is the distance from the cameras to the scene (in this case the center of the measurement volume). The ratio of δZ to δX, the size of a single voxel in physical units (mm for this study) in the Z and X-Y directions, is given by

$$\frac{\delta Z}{\delta X} \cong \frac{1}{D} + \frac{Z}{D s_0} \tag{3.4}$$

To prevent the formation of excessively elongated particles in the Z-direction, the

baseline spacing must be sufficiently large. In the current study, D = 0.33, δX = 0.0619 mm, and the focal plane spacing is resultantly set to $\delta Z \cong 0.2$ mm. The timing of data acquisition between images is set such that there is sufficient particle displacement of at least a focal plane in Z. At shorter interframe times, the SAPIV system will successfully resolve X-Y velocities, but not register particle displacement or velocity in the Z-direction.

Before refocusing, raw images are preprocessed using a procedure similar to those implemented for tomographic PIV. Preprocessing removes reflections off the fish body, enhances contrast, reduces ghosting, and improves reconstruction quality. Preprocessing consists of the following routine:

1. Subtract median-filtered image to remove fish body (5 × 5 pixel windows)
2. Convolution with a Gaussian kernel (3 × 3 pixel windows)
3. Intensity normalization with local min/max filter (10 × 10 pixel window denoted by x) according to:

$$I_{norm}(x) = \frac{I(x) - I_{min}(x)}{I_{max}(x) - I_{min}(x)} \tag{3.5}$$

4. Subtract sliding minimum (10 × 10 pixel window)
5. Implementation of the following refocusing cost function:

$$I_{FP_{ki}}(x,y) < \frac{1}{mn} \sum_{y=1}^{n} \sum_{x=1}^{n} I_{FP_{ki}}(x,y) = -1 \tag{3.6}$$

Large, high-intensity reflections and bright regions of the fish body are eliminated by subtracting a median-filtered version of the image. Similar procedures have been used by Jeon and Sung [33] and Adhikari and Longmire [1] for object removal for tomographic PIV. The Gaussian filter is used to enlarge particle image diameters for better reconstruction. Particles are small (3 pixel mean diameter) in the raw images as a result of the high numerical aperture ($f\#$) needed for sufficient depth of field to

capture the entire illuminated measurement volume. Intensity normalization over a 10×10 pixel region x in the image is performed according to eqn. 3.6 to increase the image contrast and account for variations in the laser beam intensity over the volume. This filter is especially useful in regions where the fish body reflects more light into its immediate surroundings. The sliding minimum is used to eliminate any low intensity background light amplified by the min/max filter.

Further studies on rapid particle reconstruction algorithms for multi-camera 3D PIV have introduced a multiplicative algorithm that can be used to enhance the signal-to-noise ratio of the refocused images [38]:

$$I_{SA_k} = \prod_{i=1}^{N} (I_{FP_{ki}})^n \tag{3.7}$$

In the regions nearest to the fish body, partial occlusions, where a particle is blocked in some subset of the cameras but not all, are common. The multiplicative algorithm, which requires perfect convergence of a particle in all cameras, would fail to reconstruct any particles in these crucial regions. The refocusing cost function is introduced as an alternative. This preprocessing step is a simple weighting function that penalizes the dark regions of an image where no particles exist. When summed in the additive algorithm, this serves to eliminate the background noise from each transformed image when a particle does not converge at a given location. The particle is, however, still reconstructed when it is present in more cameras than it is absent from.

The refocusing cost function is applied instead of the overall intensity thresholding performed on refocused images by Belden et al. [9]. Previous image thresholding assumed a Gaussian model for the histogram of each refocused image and removed all light below a set intensity. This process eliminated values at the edges of refocused particles in addition to noise. This method also required thresholding be performed on every refocused plane. With the cost function some computational speed is gained by thresholding only as many images as cameras (nine for the present study) instead of 100+ refocused planes. The refocusing cost function also results in a 3D Gaussian

particle (fig. 3-4), allowing for finer localization of the particle in 3D space.

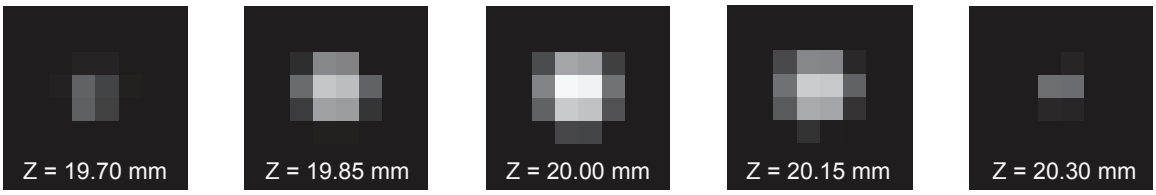

Figure 3-4: Intensity profile of a single synthetic particle refocused using the cost function over focal planes with spacing δZ = 0.15 mm. The particle center lies at Z = 20.00 mm. The particle can be represented by a 3D Gaussian kernel in voxel space and localized using this intensity distribution, analogous to a 2D PIV particle image in pixel space.

As a validation test, the cost function was first implemented on data from a synthetic camera array constructed in Blender rendering software [23]. The synthetic array simulates nine cameras spaced 150 mm apart in a 3 $\times$ 3 configuration placed 500 mm behind a tank of water. 14,000 synthetic particles were seeded over a 50 mm $\times$ 40 mm $\times$ 40 mm volume and imaged in the simulated cameras (image density N = 0.015 particles/pixel). The measurement volume begins 30 mm into the water layer, and refractive effects are considered in the camera simulation. Using the refocusing cost function, the reconstruction quality Q, defined as in [17] as

$$Q = \sum_{X,Y,Z} \frac{E_r(X,Y,Z) \cdot E_s(X,Y,Z)}{\sqrt{\sum_{X,Y,Z} E_r^2(X,Y,Z) \cdot E_s^2(X,Y,Z)}} \tag{3.8}$$

of the simulation was 0.98, successfully reconstructing almost all of the synthetic particles. Small errors in reconstruction are due to differences between the reconstructed and synthetic intensity profile. Sample raw and refocused images from the simulation can be see in fig. 3-5. The reconstructed image is sparse in each focal plane because the measurement volume is thick and ghosting is virtually non-existent in the final data. The only small, faint features present are those with centers less than two focal planes away that are fading into or out of view.

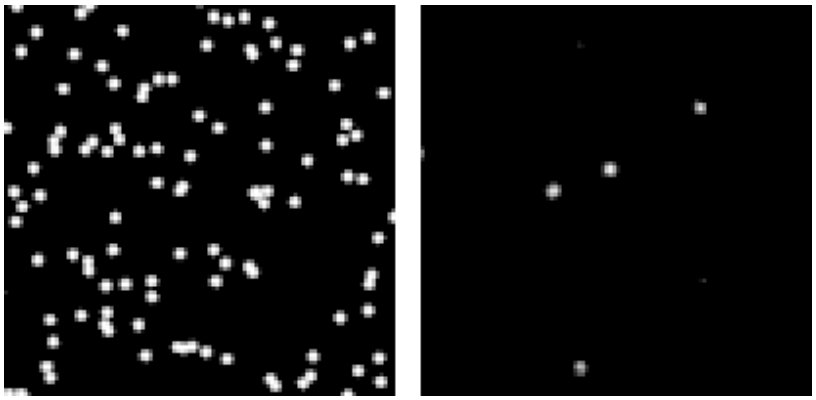

Figure 3-5: 100 × 100 pixel zoomed views of a raw image from the center camera and a refocused image at the center of the measurement volume for the reconstruction quality simulation.

3.2 Experiment Setup

Adequate reconstruction of particle fields in SAPIV requires sufficient raw data from each camera, and a large amount of attention was paid to the physical setup of the experiment (fig. 3-6) to achieve this. Experiments were conducted with the fish swimming in a five gallon tank with dimensions 400 mm × 250 mm × 200 mm. The experiment tank was filled to a water level of 160 mm with water taken from the fish's home tank. Slotted acrylic dividers were used to restrict the fish to swim in the center 300 mm of the tank in the X-direction without preventing flow from passing through. The measurement volume where all camera fields of view overlapped was 70 mm × 60 mm × 40 mm. The tank was seeded with 50 µm polyamid particles to a density of C = 230 part/cm^3, giving an image density N = 0.03 particles/pixel.

3.2.1 Cameras

The camera array consisted of nine Manta CCD cameras by Allied Vision Technologies with 1292 × 964 pixel grayscale resolution. Each camera was equipped with a 35 mm C-mount Tamron lens set to $f\#$ 5.6 to ensure sufficient depth of field for the entire measurement volume to be in focus. The Manta cameras were run at their maximum frame rate of 30 Hz and controlled using StreamPix software by Norpix. The software

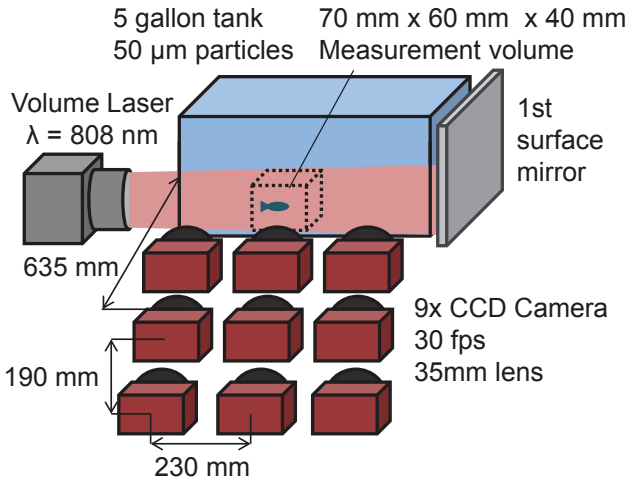

Figure 3-6: Experiment setup for SAPIV. Nine CCD cameras are arranged alongside a five gallon tank at a distance of 635 mm from the tank front and spacing of 230 mm horizontally and 190 mm vertically. A volume laser with wavelength 808 nm illuminates a measurement volume of 70 mm × 60 mm × 40 mm.

was run on a custom ASUS workstation configured by Norpix with an Intel®Core™i7 CPU, 24.0 GB of RAM, and a NVIDIA GeForce®210 graphics card. Each camera transmits data to the computer via a gigabit Ethernet connection. To prevent frame dropping, all data is stored on the computer's RAM during acquisition and then exported to the hard drive after the run has finished. For maximum image quality, all data was exported as both StreamPix RAM sequences and TIFF files.

The array was positioned 635 mm from the front of the tank in a 3 × 3 arrangement with 230 mm horizontal spacing and 190 mm vertical spacing between cameras. The cameras are each mounted on a Giottos MH-1002 ballhead tripod head to enable easy adjustment. All cameras are attached to a custom 80/20 aluminum frame (fig. 3-7) to enable height adjustment of the overall array and view angle adjustment of the top and bottom camera rows.

3.2.2 Illumination

Illumination is provided by a 1000 W Oxford Lasers Firefly Volumetric Laser with 808 nm wavelength. The laser was pulsed in sync with the cameras at a constant inter-frame time $\Delta t = 0.033$ s. While this interval is higher than usually implemented with

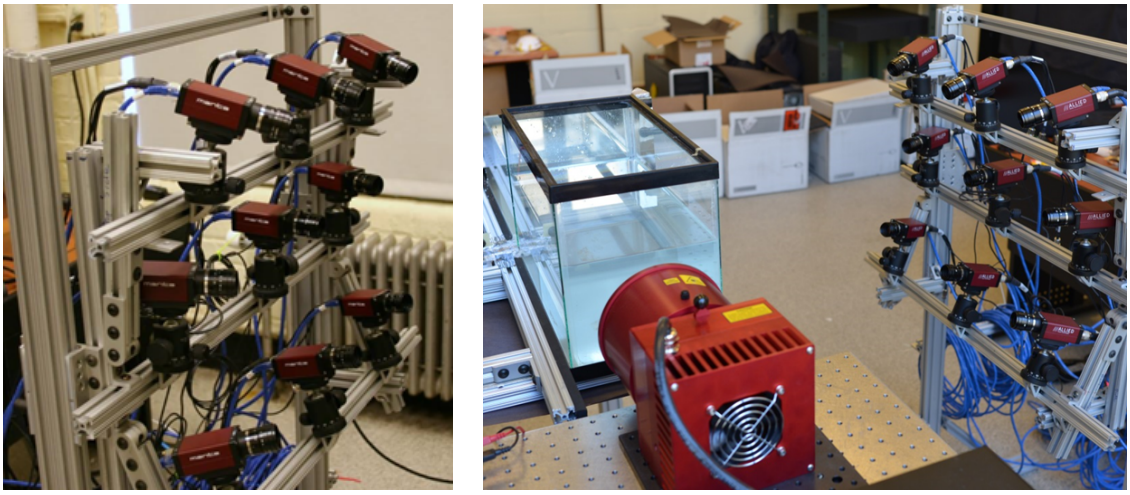

(a) (b)

Figure 3-7: **a** Camera array mounted on a custom 80/20 frame. **b** Position of the camera array relative to the tank in the experiment setup used for SAPIV.

conventional frame-straddling, this was necessary for resolvable particle displacement of at least a focal plane (0.2 mm) in the Z direction. The laser pulse duration was kept short at 50 µs to eliminate any motion blur in the images. Timing between the cameras and the laser was provided by a Berkeley Nucleonics Corporation Model 505 delay generator.

Sufficient illumination was a substantial experimental challenge. Image brightness and $f\#$, the ratio of a lens's entrance pupil diameter to focal length, are inversely related. The high $f\#$ required for the entire volume to be in focus limited the amount of light in the overall image. In addition, the light sensitivity of the sensor in the CCD camera is wavelength dependent. The quantum efficiency, a measure of what percentage of photons hitting the sensor register a charge, is over 50% at $\lambda = 532$ nm, but is barely over 20% at $\lambda = 808$ nm. Furthermore, the intensity of light traveling through a medium will decay according to the Beer-Lambert law:

$$I = I_0 e^{\alpha x}, \tag{3.9}$$

where I is the light intensity at a given location in the volume, I_0 is the initial intensity of the light as it enters the medium (in this case water), x is the distance into the

medium traveled, and α is an absorption coefficient. Hale and Querry [29] found that the absorption coefficient α for light at 808 nm is $\alpha = 0.022$ cm^{-1}, while at 532 nm $\alpha = \ = 0.0035$ cm^{-1}. Since near-IR attenuates almost an order of magnitude more than the green light (e.g. 532 nm) typically used for PIV in water, a first surface mirror was placed at the end of the tank to reflect the beam back into the volume. The laser attenuation over the dimensions of the experiment tank is demonstrated in fig. 3-8. Given the attenuation, further mirrored passes of the beam, as done by Ghaemi and Scarano [25] for amplification of green light within a volume, would not provide significant additional illumination.

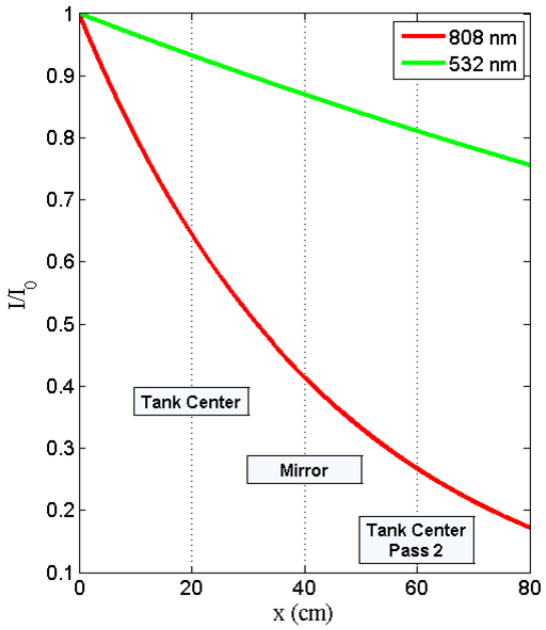

Figure 3-8: Laser attenuation over the measurement volume at 808 nm and 532 nm.

Index of refraction is a wavelength dependent property. In room temperature (25°C) water, the index of refraction at $\lambda = 808$ nm is n = 1.329, and at $\lambda = 532$ nm is n = 1.334 [29]. As a result cameras also had to be calibrated using illumination at a wavelength close to that of the laser. The calibration light source was an array of LEDs with wavelength $\lambda = 850$ nm, still yielding n = 1.329 according to the correlation Hale and Quarry provide.

3.2.3 Processing

Refocusing and PIV processing were performed on a Dell XPS 8300 workstation with an Intel® Core™ i7-2600 CPU, 8.00 GB of RAM, and an AMD Radeon™ HD 6700 Series graphics card. The velocity fields were processed using a multipass normalized cross-correlation in a modified version of MatPIV [65] adapted for 3D use. Correlation window sizes were 128 × 128 × 32 voxels for the first pass and 64 × 64 × 16 for the second two passes, all with 50% overlap between interrogation windows. The windows were sized such that the X, Y, and Z dimensions of each window were close to equal. For each window, the correlation function was evaluated as

$$R(s,t,u) = \frac{\sum_{m=0}^{M-1}\sum_{n=0}^{N-1}\sum_{p=0}^{P-1} I_1^{i,j,k} \cdot I_2^{i,j,k}(m-s, n-t, p-u)}{\left[\sum_{m=0}^{M-1}\sum_{n=0}^{N-1}\sum_{p=0}^{P-1} I_1^{i,j,k}(m,n,p)^2 \sum_{m=0}^{M-1}\sum_{n=0}^{N-1}\sum_{p=0}^{P-1} I_2^{i,j,k}(m-s, n-t, p-u)^2\right]^{1/2}}, \tag{3.10}$$

where R is the cross-correlation function value, I_1 and I_2 are the grayscale intensity volumes of each window in successive images, M, N, and P are the overall dimensions of the window, m, n, and p are the specific coordinates of each voxel, and s, t, and u are the XYZ displacements in voxels between timesteps. The convolution operation in the correlation function was evaluated as multiplication in the frequency domain by first taking the 3D zero-padded fast Fourier transform (FFT) of both interrogation windows (I_1 and I_2) using the MATLAB function "fftn".

The final resolution was a velocity vector every 1.85 mm in X and Y and every 1.60 mm in Z. After processing, the velocity field was post-processed using a filter based on the height ratio between the correlation peak and the second-highest peak (threshold 1.3) and a local median filter that removed vectors further than two standard deviations away from the mean velocity of a 3 × 3 × 3 window neighborhood. Filtered vectors were replaced using iterative linear interpolation. Interpolation begins at the points surrounded by the most valid vectors and fills in the vector field

until all regions outside the mask are complete. Approximately 5% of the total vectors in the volume were replaced by post-processing. Before computing vorticity, the velocity field is smoothed once with a 3 × 3 × 3 Gaussian kernel. Vorticity is calculated using a centered difference approximation between neighboring vectors

$$\omega_k(m,n) = \frac{u_i(m+1,n) - u_i(m-1,n)}{2\delta x_i} - \frac{u_j(m,n+1) - u_j(m,n-1)}{2\delta x_j} \tag{3.11}$$

where ω_k is the vorticity vector component, u_i and u_j are the velocity components in the orthogonal directions, δ_i and δ_j are the spacings between vectors in each direction, and m and n are the indices of a specific vector. Alternate methods of calculating the vorticity, such as those compared by Luff et al. [45] require sampling larger neighborhoods of velocity vectors, thus reducing the spatial resolution of the measurement.

3.2.4 Validation

The SAPIV system was validated with a benchmark experiment of a vortex ring generated by a mechanical piston. The validation experiment performed is similar to that of Belden et al. [9], but with a modified setup. Validation was necessary to assess the impact of several advances in experiment execution and processing made since the preliminary SAPIV experiments performed at MIT. The vortex piston used in this study is a modified syringe, with diameter D_{outer} = 26 mm, orifice diameter $D_{oriface}$ = 17 mm, stroke length L_{stroke} = 10 mm and stroke velocity U_{piston} = 20 mm/s. The ratio of $L_{stroke}/D_{oriface}$ is 0.59. As seen in fig. 3-9, slices of the ring velocity field taken at several angles about the center axis show the expected form, an axisymmetric ring with a downward center thrust jet. The slice planes chosen for analysis coincide with the velocity vector spacing.

The circulation in the ring was also used to characterize the uncertainty of the impulse measurements derived from SAPIV data. Over short timescales in which viscous interactions are negligible, the vortex ring must obey Kelvin's circulation theorem:

$$\frac{D\Gamma}{DT} = 0 \tag{3.12}$$

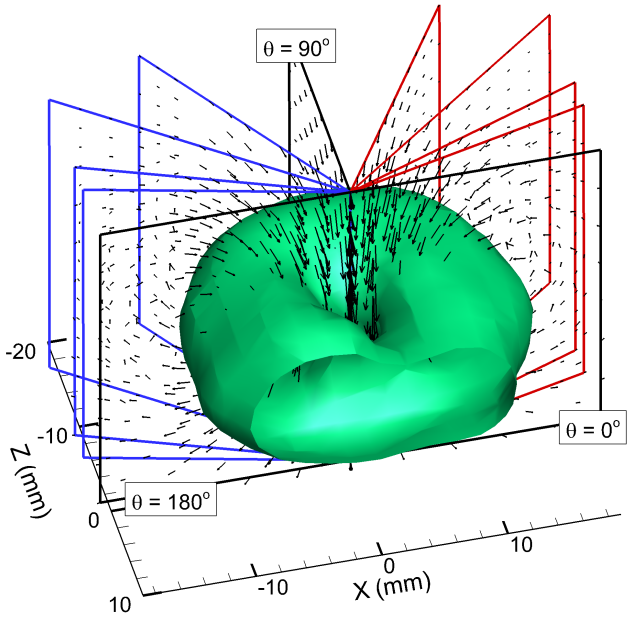

Figure 3-9: Velocity vectors at each slice through the vortex ring used to determine circulation. The isovorticity contour is drawn at 25 s^{-}1, 33% of the peak vorticity magnitude. Every other vector in y is shown for clarity. Using the coordinate system shown on the on-axis slices, the off-axis slice planes, stepping with the vector grid, are located at $\theta = 15.0°, 21.9°, 38.8°, 58.2°, 121.8°, 141.2°, 158.1°$, and $165.0°$.

This requires that the circulation measured at any slice through the ring is consistent with the values measured on other planes. As shown in fig. 3-10, the circulation, taken at each slice through the ring along rectangular contours of increasing enclosed area until the value plateaued or dropped, demonstrates good agreement with Kelvin's theorem. Prior to calculating circulation, the velocity vectors were linearly interpolated onto a 1 mm cubic grid so that the integration contours in each slice would have the same enclosed areas. The peak circulation value is $\Gamma = 62.47 \pm 1.36$ cm^2/s (2% variation).

Uncertainty analysis was also performed on the geometric aspects of the ring. Since the vortex ring generated extended slightly beyond the measurement volume, radius had to be measured instead of diameter. All radii were measured from the geometric center of the ring as determined from the isovorticity contour shown in fig. 3-9. The measured ring radius is R = 1.15 ± 0.05 cm (4% variation), and vortex core diameter $D_0 = 1.10 \pm 0.20$ cm (18 % variation). These dimensions resulted in an

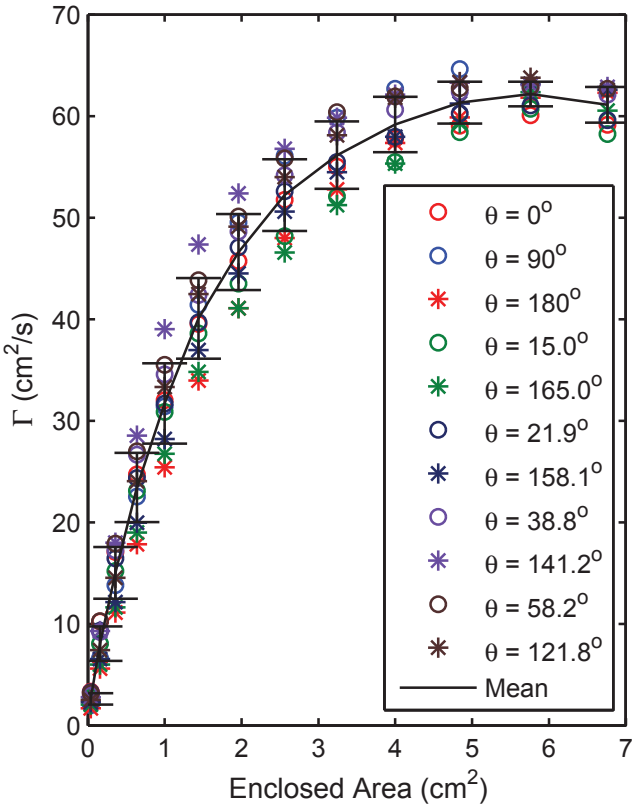

Figure 3-10: Circulation magnitude calculated by eqn. 2.5 on each of the slice planes seen in fig. 3-9. Error bars show one standard deviation in the circulation value for each enclosed area. The mean maximum value of circulation across all the planes is 62.47 cm^2/s and is seen at an enclosed area of 6 cm^2.

impulse calculation of 262 ± 23 g $\cdot$ cm/s, approximately 10% uncertainty on the final impulse measurement.

3.3 Fish

The species of fish used in this study is the Giant Danio *(Danio aequipinnatus)*, a larger relative of the common laboratory Zebra Danio. PIV was performed on five fish during the study. Anderson [4], Wolfgang et al. [74], and Epps and Techet [18] have all previously performed 2D PIV on the Giant Danio, and Zhu et al. [75] presents a three-dimensional numerical model of this species for comparison. Results are presented for a fish with body length L = 58 mm, mass M = 4.8 g, and tip to tip

caudal fin width W = 12 mm.

The Giant Danio were housed in a 30 gallon aquarium in the lab. For experiments, one fish was moved to the five gallon experiment tank. To prevent animal stress, the water used for experiments was taken from the home tank of the fish right before beginning tests. Prior to testing, the fish was also weighed in a small acrylic box also filled with home tank water. The box was filled to a water level of 1-2 cm, weighed, and then weighed again after the fish was placed in the box. The box had a 2 mm chessboard grid background attached to one side. The fish body length was measured by photographing the fish against this background and counting the number of grid squares from nose to caudal fin tip. Body length was verified using refocused data images where the entire fish body was in the camera field of view. All animal procedures were performed under the regulation of the MIT Committee on Animal Care and Department of Comparative Medicine.

In order to achieve sufficient baseline spacing for resolvable particle displacements in the Z-direction, the camera array had to be positioned close to the tank with relatively wide distance between cameras. Thus, the fish body occupied a large portion of the field of view, and tracking the body over large time sequences (more than 10-15 images) was not possible without restricting the fish to swim in an unnaturally small area. This constraint was not desirable as it would generate irregular swimming behaviors not of biomimetic interest. As a result, the mean body velocity was determined only over short time sequences. Velocities presented here were measured over the duration of time in which the fish body was in view by tracking the 3D motion of the fish eye in refocused raw images.

The Strouhal number, defined as

$$St = \frac{fA}{U} \tag{3.13}$$

where f is the tailbeat frequency in Hz, A is the double amplitude of the caudal fin, and U is the body velocity, was determined by manually tracking the fish eye and the two tips of the caudal fin. The path of the eye was used to determine the

mean body velocity, while the amplitude of the tail beat was determined from the 3D position of the two caudal fin tips. Even within a single run, inconsistency in amplitude and velocity was observed as a result of stroke-to-stroke variation in the fish's kinematics. Strouhal numbers presented here represent averaged values. Fish body tracking algorithms for synthetic aperture imaging are the focus on ongoing work.

3.4 Fish Body Reconstruction

Numerous studies have shown the importance of masking PIV data to obtain an accurate velocity field near a solid body. Since the fish is arbitrarily moving, it is also necessary to reconstruct the fish body to understand the relationship between its kinematics and the wake it creates. Kim and Gharib note that the 3D shape of a vortex ring generated by a paddling propulsor varies with the shape of the propulsor [36], suggesting that fin conformation during vortex generation on a fish body must be known to determine its influence on the wake. Fig. 3-11 shows the raw images from all nine cameras during one forward swimming sequence. It is clear that no single camera can fully describe the 3D position and shape of the fish body.

When experiments are run in a controlled flume, such as those performed by Flammang et al. using DDPIV, the location of the caudal fin remains consistent enough for use of the same mask throughout the run [22]. In contrast, the fish in this study is moving freely, requiring a new mask for each image pair. Given the large number of cameras, defining the mask manually is also less than ideal, resulting in the development of an automated masking procedure.

The masking technique for SAPIV is based on the visual hull method used for tomographic PIV developed by Adhikari and Longmire [1]. First, the fish body must be identified in raw images from each camera at each timestep. Several methods for PIV image segmentation were tested for this purpose. Jeon and Sung [33] use filtering based on scattered small high intensity peaks within an image to separate particles from an arbitrary background for tomographic PIV, a technique dependent

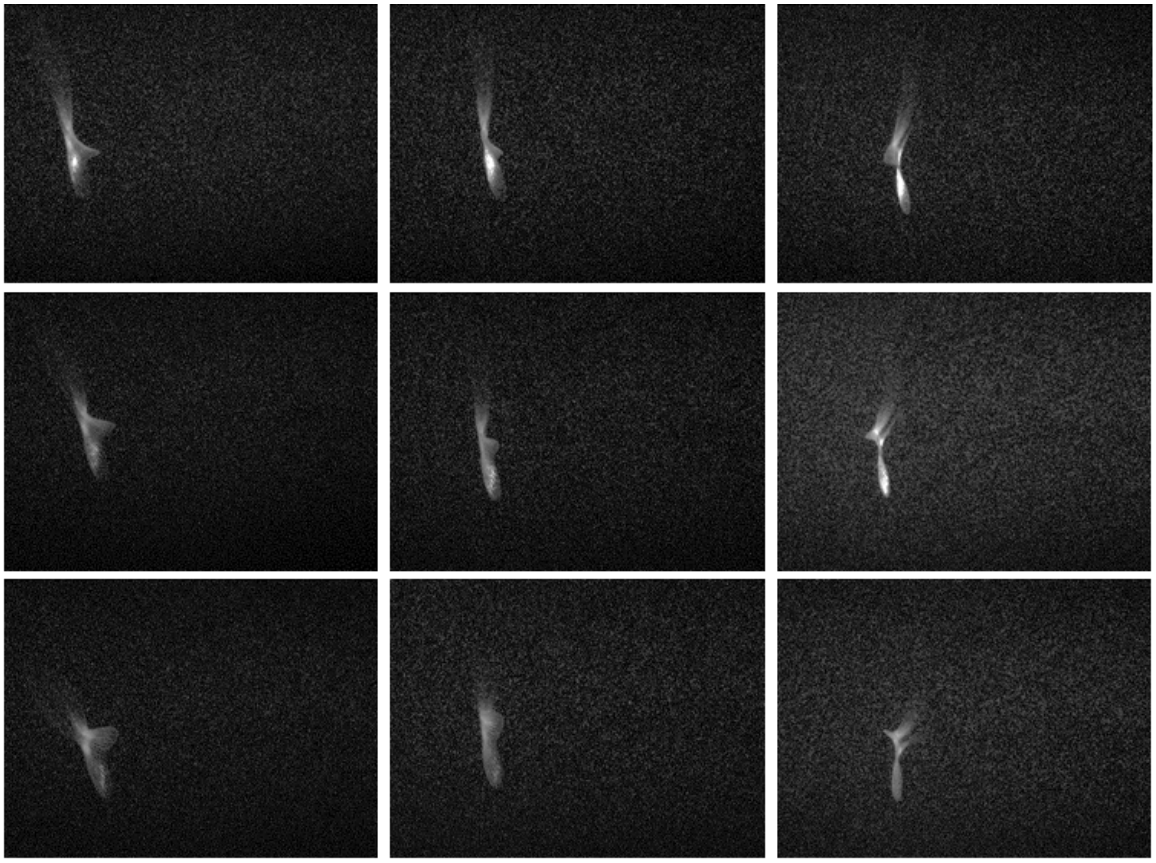

Figure 3-11: Raw images from all 9 cameras for an instance of forward swimming. No single image provides a complete description of the 3D swimming kinematics. Contrast has been enhanced for body visibility.

on high intensity contrast between the particles and a much fainter background. In this study, reflections along the body were frequent and created high intensity image regions along the body other than particles. These algorithms also struggled to detect both bright and dark regions of the fish body. An edge detection procedure and morphological operations can also be used to remove objects as outlined by Adhikari and Longmire [1]. Applications of edge detection to the data in this study failed because the numerous markings on the Giant Danio body created spurious edges within the raw images.

To address the body patterning of fish scales, Siddiqui [61] introduced an adaptive thresholding algorithm specifically for fish. The image is segmented by separately extracting both bright and dark portions of the body while minimizing coalesced particles and stitching the two partial masks together morphologically. A similar

algorithm was implemented here, with changes in the initialization threshold and morphological filter sizes made to account for the volume illumination and specific body size and markings of the fish in this study. A flowchart of the masking routine is presented in fig. 3-12.

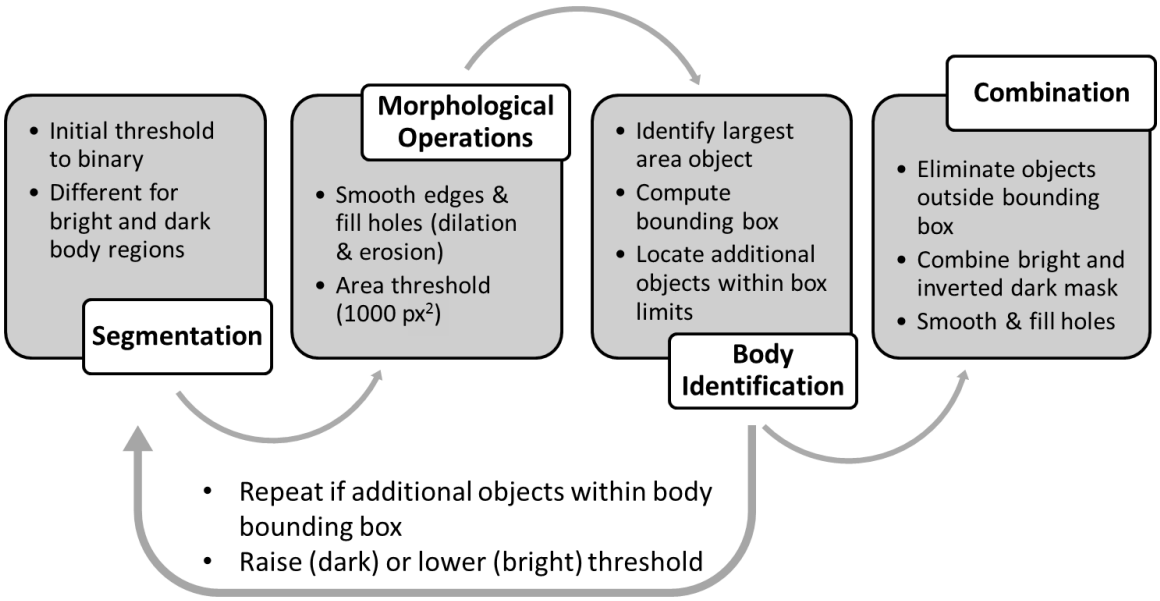

Figure 3-12: Flowchart of the thresholding algorithm used for mask generation

Before segmentation, the illumination was equalized across each image through a Contrast-Limited Adaptive Histogram Equalization (CLAHE) operation in MATLAB. The initial intensity threshold (0 to 1 normalized grayscale values) for the bright body segments was 0.12, and for the dark segment was 0.15. The morphological operations performed after segmentation for bright mask extraction consisted of:

1. Image erosion (3×3 pixel square mask)
2. Image dilation (3×3 pixel square mask)

For the dark mask the routine was:

1. Image dilation (5×5 pixel square mask)
2. Image inversion

3. Image erosion (5 × 5 pixel square mask)

After adding the final bright and dark segments together, the images are smoothed by:

1. Image dilation (10 × 10 pixel square mask)
2. Fill all internal holes in image
3. Image dilation (5 × 5 pixel square mask)
4. Fill all internal holes in image
5. Image erosion (5 × 5 pixel square mask)
6. Image erosion (10 × 10 pixel square mask)

Raw masks extracted from all nine cameras can be seen in fig. 3-13.

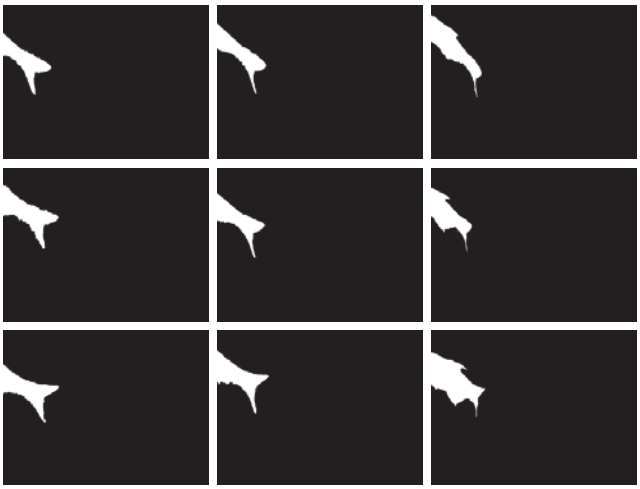

Figure 3-13: Binary mask images from all nine cameras (arranged the same as the physical camera array) show several different silhouettes of the caudal fin as the fish swims across the tank.

Siddiqui reports a success rate of greater than 90% using this algorithm [61]. The estimated success rate on SAPIV data is 93% for all processed data where the fish is entirely within the measurement volume. The most common error was when the body had almost completely passed through the measurement volume and coalesced

particles were initially detected as the most likely object to be the fish body. These masks were corrected manually before continuing with refocusing.

Raw mask binary images are then refocused using a multiplicative algorithm,

$$I_{SA_k} = \prod_{i=1}^{N} I_{FP_{ki}}, \tag{3.14}$$

to determine where all masks overlap on a given focal plane. This represents the portion of the body that physically occupies each plane, as shown in fig. 3-14.

Figure 3-14: Three slices of the refocused mask. One tip of the caudal fin lies at roughly Z = -2.0 mm, the second tip at Z = 6.0 mm, and the caudal peduncle at Z = 14.0 mm.

These focal planes can be stacked to determine a visual hull of the fish body in the 3D volume (fig. 3-15).

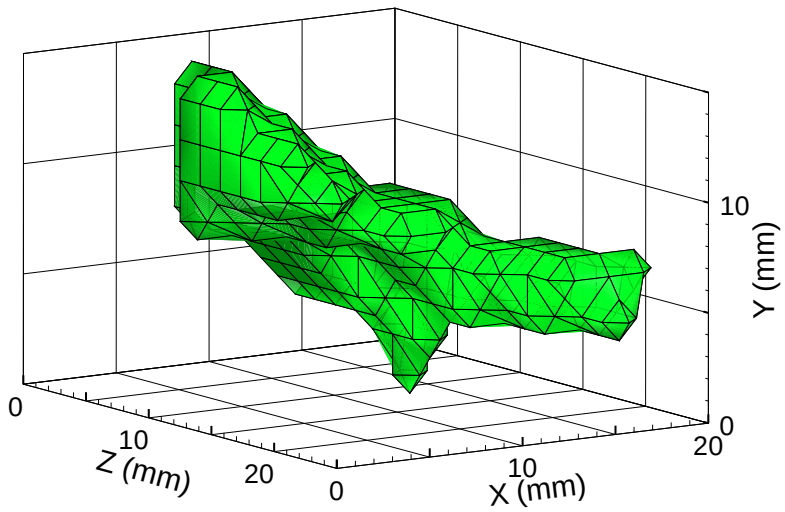

Figure 3-15: Reconstructed caudal fin visual hull from the refocused mask planes.

During the 3D cross-correlation step of SAPIV processing, if the midpoint of an interrogation window falls within the coordinates of the visual hull, it is included as part of the mask. Masked voxels are excluded from velocity calculation and treated as a region in which no velocity vectors can pass through.

The masking technique was validated by dropping small spheres of varied surface reflectance into the tank. A sample of the reconstructed mask for a white plastic sphere of diameter 16 mm can be seen in fig. 3-16. The masking code successfully reconstructs the object in the flow and also prevents velocity vectors from passing through the solid body. Similar results were observed using a clear sphere of the same size. Reflection and image bloom were a consistent problem when validating the masking code on a metallic reflective sphere, but the fish body proved to be much less reflective than this object.

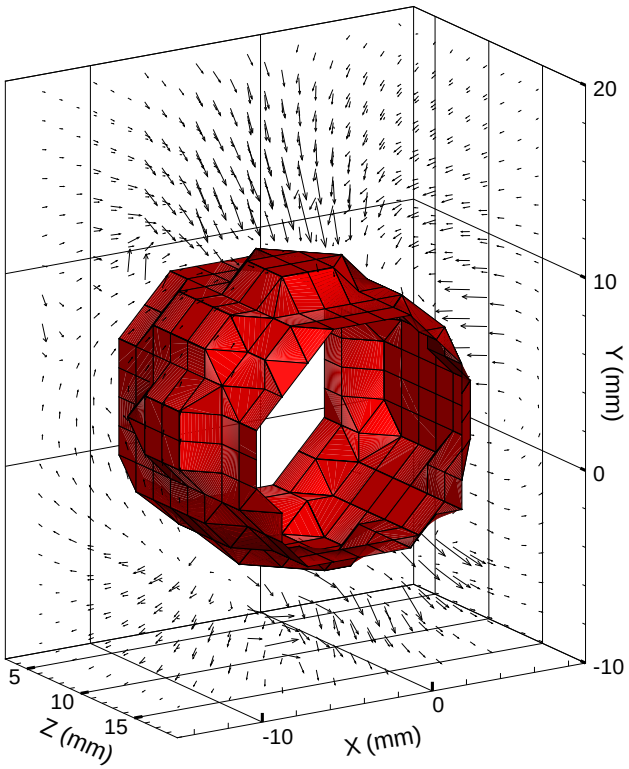

Figure 3-16: Validation experiment for the masking technique. A sphere with diameter 16 mm is dropped into the tank and imaged using SAPIV.

The baseline spacing of the camera array during the masking experiments was approximately D = 0.20. As a result, the particles are elongated in depth and Z-

displacement could not always be resolved. Particle elongation creates spurious vectors with purely X-Y velocities in the SAPIV-processed field. The baseline spacing also resulted in the formation of an elongated spherical mask that extended beyond the actual diameter of the sphere. While the depth extents can be limited by increasing the baseline spacing, some blur is always created by the overlap of images at locations close to, but not on, the focal plane of convergence. This blur will always cause some elongation in Z beyond the actual depth of the sphere. Scharfman et al. [58] describes synthetic aperture reconstruction of binary dark field images of spherical droplets and reports the error in measuring the sphere's radius as a result of the false convergence created by the blur. For spheres between 0 mm and 40 mm in radius, the error in radius measurement is less than 4% in all camera simulations. With sufficient baseline spacing, similar amounts of elongation are expected for the fish body.

Chapter 4

Analysis of Fish Wake Dynamics using Volumetric PIV Data

Allowing the fish to swim freely enabled SAPIV measurements to be obtained for a variety of fish behaviors and swimming speeds. Results will be presented for cases of forward swimming at two speeds, 1.00 and 1.38 bodylengths/second (L/s), and a 75° turning maneuver. For each of these behaviors, the 3D structure of the wake is visualized and circulation and impulse are calculated. In the cases of faster forward swimming and turning the circulation and impulse are also measured over several consecutive timesteps to determine how quickly the wake features of these faster maneuvers break down in an otherwise static tank. The energy balance between the fish and its wake must be considered when the wake is at full strength and energy has not dissipated into the water outside the vortex. The timescale over which such analysis can be conducted is an important design concern for future SAPIV experiments on fish.

4.1 Forward Swimming

4.1.1 Single Vortex Ring

Results are first presented for the simplest swimming scenario possible: steady forward swimming at relatively low speed. Survey images from the center camera of the array at three timesteps can be seen in fig. 4-1. The fish is swimming roughly in the Z-direction into the tank at a speed U = 1 L/s.

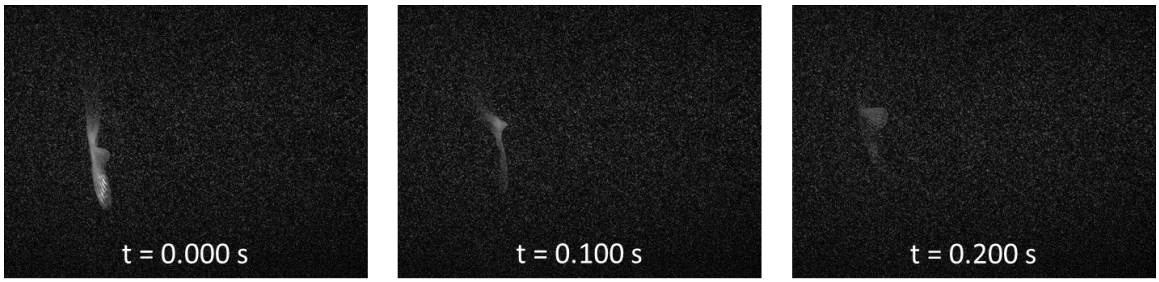

Figure 4-1: Raw images from the center camera as the fish swims back into the tank. Contrast has been enhanced for body visibility.

The tailbeat frequency is $f = 3.33$ Hz and the double amplitude is 5.9 mm, giving St = 0.34, within the range of 0.25 - 0.4 determined by Trinatafyllou et al. to be optimal [67]. The Reynolds number of the fish, defined with respect to the body length of the fish L and mean body velocity U as

$$Re = \frac{\rho U L}{\mu} \tag{4.1}$$

was approximately 3300.

Reconstruction of the wake behind the caudal fin shows a single vortex ring behind the fish with the axial thrust jet in the ring's center moving away from the lower tip of the caudal fin (fig. 4-2). The maximum velocity in the ring is 36.2 mm/s (0.62 L/s), located in the center of the jet. The peak vorticity magnitude in any X-Y plane is 10.7 s^{-1} and in any X-Z plane is 9.9 s^{-1}.

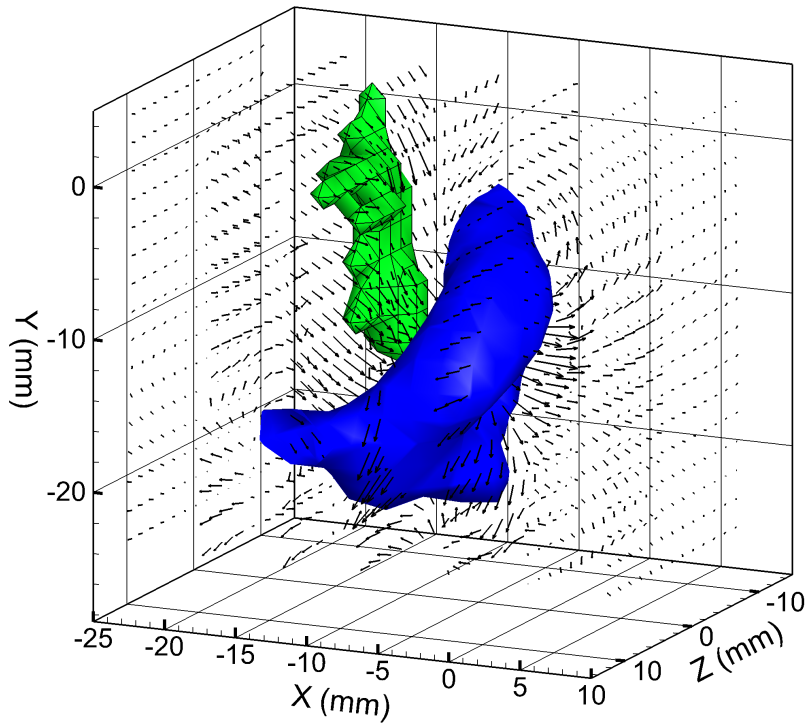

Figure 4-2: A single vortex ring behind the fish during forward swimming at U = 1 L/s. The isovorticity contour is drawn at 5 s^{-1}. Velocities are largest in the center of the ring, which is aligned with the lower tip of the caudal fin. The peak velocity magnitude is 36.2 mm/s (0.62 L/s). Every third vector along the X-axis is plotted for clarity.

For the single vortex ring reconstructed during 1 L/s swimming, the ring geometry and circulation are analyzed on four slices through the wake ring taken about the ring center. Tangent velocity vectors and the vorticity magnitude of each slice used can be seen in fig. 4-3.

Following Drucker and Lauder's procedure for vortex ring analysis [15], the ring orientation, diameter D, and core diameter D_0 are measured using velocity profiles through the ring on each plane. The velocity vectors are transformed to the reference frame of the vortex cores [62], and diameter is measured as the distance between zero crossings of the axial velocity profile on a slice taken through the centers of the two cores. The vortex core diameter is measured as the distance between minimum and

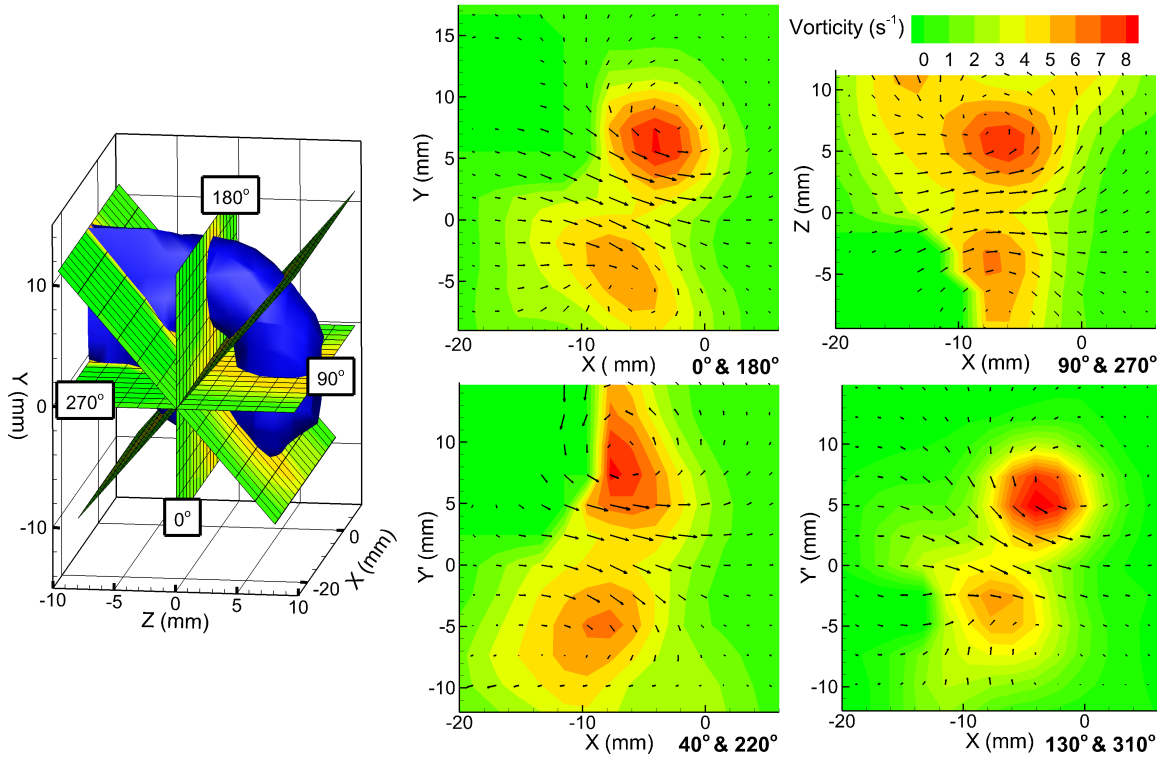

Figure 4-3: Slices of the ring used to determine circulation. The ring is sampled at locations along the X-Y and X-Z planes, as well as two off-axis cuts along the vector grid parallel to the outward normal of the ring. For each slice location, velocity vectors tangent to the plane and contours of the vorticity magnitude are displayed.

maximum tangential velocity on slices through each of the two core centers on the plane. The mean of the two measurements is taken as the overall core diameter for the slice. All 2D slices through the volume are taken about the X-axis, and thus the ring and jet orientation are taken with respect to it. The ring angle ϕ is measured positive from the horizontal axis while the jet angle α is measured negative from the horizontal axis in each slice as done by Müller et al. [49] and demonstrated in fig. 4-4.

Volumetric velocity data is also used to completely determine the orientation of the center jet. In the absence of a freestream flow or a complete fish body to determine orientation, the angle of the vortex ring and angle of the center jet are both measured relative to the tank geometry. The jet angle is measured using directional cosines at the location of the peak velocity magnitude. The angle determined with the X-axis by this method is 22°, higher than the angles found with the same axis in planar

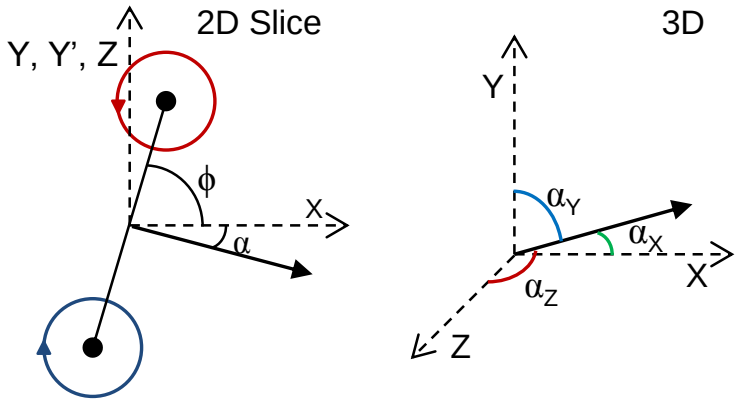

Figure 4-4: Coordinate systems used to measure the 2D orientation of the vortex ring and center jet and the 3D orientation of the center jet.

slices.

Table 4.1 summarizes the values determined for diameters, circulation, and impulse in the vortex ring. The mean diameter is 1.55 cm and the variation among the slices in diameter across all planes is no more than 11%, indicating that the ring can be treated as axisymmetric. The mean core diameter is 0.99 cm with a maximum variation of 14% in any overall plane.

Table 4.1: Diameter, circulation and impulse measured in the fish wake during forward swimming at U = 1 L/s. All properties in the final row are mean values except for the jet angle, which is measured from the X-axis in 3D instead of in 2D on a single plane.

Slice	Ring Angle	Jet Angle	D (cm)	D_0 (cm)	Γ (cm^2/s)	I (gcm/s)
0° & 180°	79°	19°	1.45	0.85	4.91	8.11
40° & 220°	82°	16°	1.72	1.05	5.04	11.71
90° & 270°	83°	5°	1.56	0.95	4.17	7.97
130° & 310°	77°	19°	1.47	1.10	4.69	7.96
Overall/Mean	-	22°	1.55	0.99	4.70	8.94

The mean circulation is 4.70 cm^2/s with a maximum of 11% variation on any plane and 20% variation in any single vortex core. The peak circulation value falls at enclosed areas between 1.96 cm^2 and 4.00 cm^2. Using the diameter and mean

circulation magnitude for each slice, the impulse calculated ranges from 7.95 to 11.74 gcm/s. The low circulation value measured on the center X-Z plane (slice angles 90° & 270°) is likely due to incomplete capture of the ring in this direction. The complete vortex cores extend beyond the volume, as can be seen in fig. 4-3, where the isovorticity contour clearly extends beyond the volume in the -Z direction.

4.1.2 Linked Vortex Rings

When the fish swims at a higher speed, the vortex cores of consecutive rings merge at points of overlap and linking occurs. This phenomena has previously been observed in 2D by Drucker and Lauder on bluegill sunfish swimming at speeds of 1.0 and 1.5 L/s [15]. Results here show prominent linking when the fish swims at a speed U = 1.38 L/s. In this case, tailbeat frequency increases to f = 5.0 Hz, while the double amplitude of the caudal fin decreases to A = 4.5 mm, giving St = 0.28. The combination of higher frequency vortex ring release and closer proximity of the rings causes cores to overlap and link.

For this run, the fish is swimming at an angle with the tank (fig. 4-5), maximizing the amount of wake visible in the measurement volume but placing the features at off-axis orientations.

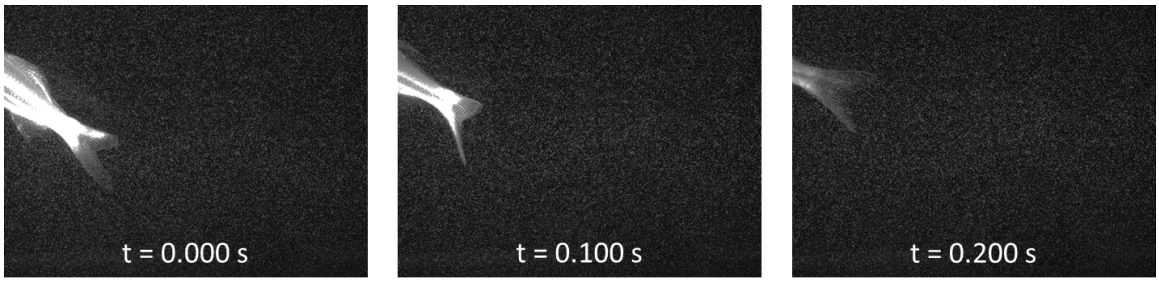

Figure 4-5: Survey images from the center camera when the fish swims at 1.38 L/s. Contrast has been enhanced for clarity.

As a result of the swimming orientation, the field of view accommodates three linked vortex rings (fig. 4-6). It is possible to track the circulation in each ring as a function of time, which is measured from when the first vortex ring is released by the caudal fin and closes on itself.

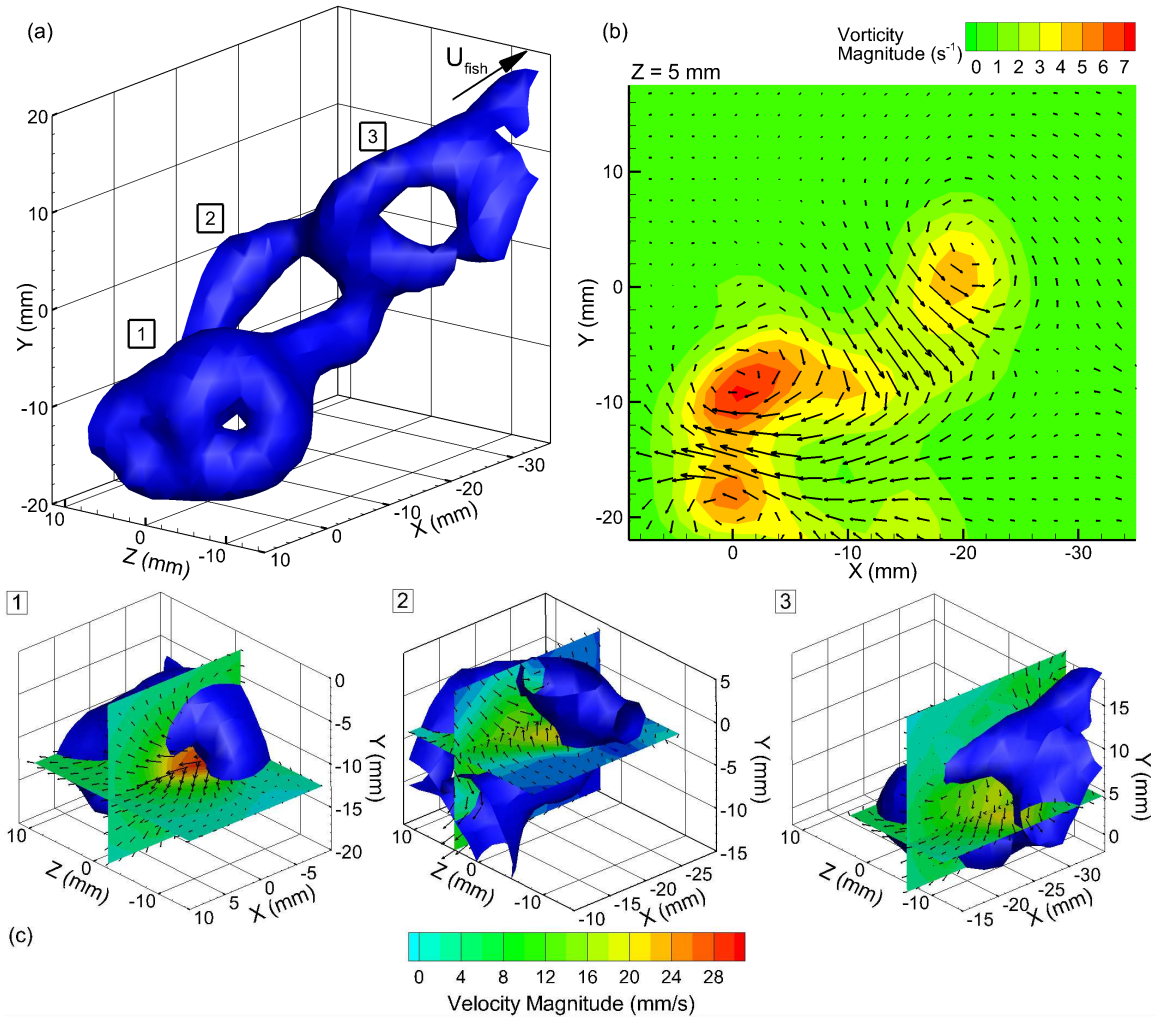

Figure 4-6: **a** Linked wake vortex rings observed at a swimming speed of U = 1.38 L/s at t = 0.233 s. The swimming direction of the fish is indicated by U_{fish}. The isovorticity contour is drawn at 4 s^{-1}. **b** Single slice illustrating the phenomena of vortex ring linking in the X-Y plane at Z = 5 mm. The cores for rings 1 and 2 have merged into a single core of higher vorticity magnitude and larger size. **c** Velocity slices through each individual ring showing the alternating orientation of the jets through the ring centers and the points of peak velocity magnitude in the center of each ring.

Since the wake features appear in arbitrary locations, the geometry and orientation of the rings are first analyzed by taking slices of the ring about each axis in the tank frame. The full 3D orientation of the ring is measured using the angles between the two vortex cores and the axes in slices through the X-Y (ϕ_X), Y-Z (ϕ_Y), and X-Z planes (ϕ_Z). The coordinate system for the orientation of the ring, shown on the

first ring in the linking system, is demonstrated in fig. 4-7. For the ring orientation measurement, no distinction is made between the positive and negative vorticity core. This aspect of the orientation is conveyed with the jet angle, which is measured in the 3D coordinate frame of fig. 4-4 using directional cosines.

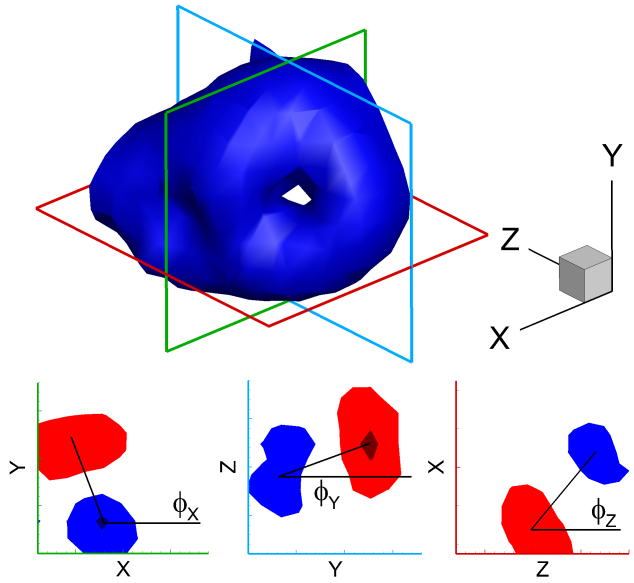

Figure 4-7: Coordinate system for measuring the orientation of the vortex rings in 3D.

Table 4.2: Size and peak jet velocity of the linked rings observed during fast forward swimming at U = 1.38 L/s.

Ring	$\lvert U_{max} \rvert$	D_{XY} (cm)	D_{XZ} (cm)	D_{YZ} (cm)	$D_{0,XY}$ (cm)	$D_{0,XZ}$ (cm)	$D_{0,YZ}$ (cm)
1	0.53 L/s	1.51	1.98	1.59	1.45	1.84	1.26
2	0.43 L/s	1.96	1.77	1.42	1.18	0.97	1.24
3	0.43 L/s	1.60	1.75	1.32	0.86	0.85	0.91

The ring diameters and vortex core diameters are also measured in slices about each axis. Geometric characteristics of the ring are summarized in Table 4.2 (diameters) and Table 4.3 (orientation). Depending on the slice plane, the ring diameter varies by as much as 24% of the mean diameter for each ring. The core diameter varies by up to 58% of the mean for each ring. These measurements demonstrate the large

Table 4.3: Orientation of the linked rings observed during fast forward swimming at U = 1.38 L/s.

Ring	ϕ_X	ϕ_Y	ϕ_Z	α_X	α_Y	α_Z
1	105°	30°	42°	43°	86°	137°
2	149°	62°	142°	133°	125°	64°
3	77°	145°	140°	47°	91°	137°

amount of uncertainty from geometry alone that planar measurements introduce into wake analysis.

For each vortex ring, the circulation was determined on the same four slice planes as the single vortex ring previously seen in fig. 4-3. At slices where multiple rings link and share a core, such as the vortex in the X-Y plane of ring 1 seen in fig. 4-6b, the vorticity magnitude and computed circulation are much higher than in the opposite section of the same ring. Since circulation is taken as an integral of velocity, the additional velocity contribution of the second ring is responsible for the observed lack of conservation of circulation.

Measures of the circulation over time in each ring can be seen in fig.4-8. In ring 1 (fig. 4-8a), the first ring shed by the fish, the slices at 139 ° and 180° show notably higher circulation values than the other slices. Perpendicular to the linking, at 90° and 270°, the circulation values are much closer to conserved. There is a maximum of 8% deviation from the mean of the two cores found at t = 0.033 s. In ring 2 (fig. 4-8b), the circulation at 0° peaks at t = 0.000 s and closely follows the trend seen in ring 1 at 180° as a result of linking of the vortex cores. Circulation at 139° increases with time as ring 3 forms, is shed, and links with ring 2 at this location. The planes perpendicular to the linking are again the closest to conserved, with a maximum of 24% difference at t = 0.100 s in the 90° and 270° plane and 20% difference at t = 0.200 s in the 40° and 220° plane. In ring 3 (fig. 4-8c), the slice at 319° links with ring 2, and the circulation peaks at t = 0.167 s when this side of the ring is first shed. Circulation values at 40°-220° consistently increase over time as the ring is released by the fish.

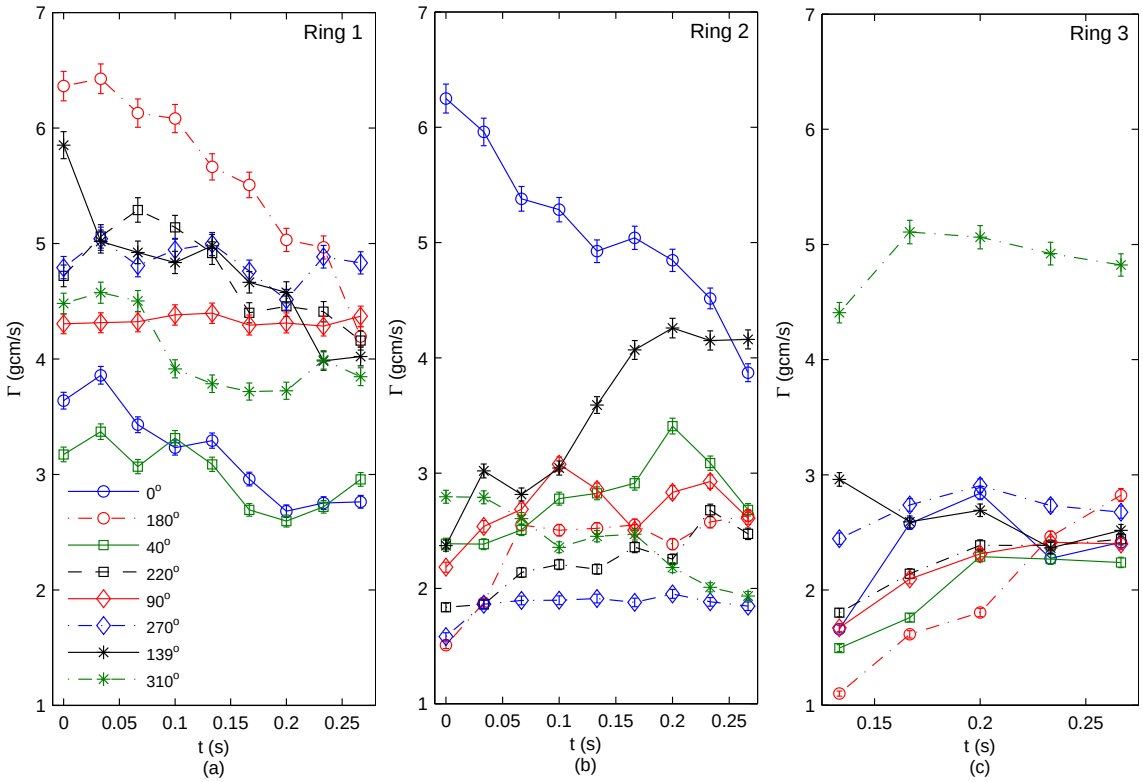

Figure 4-8: Circulation over time in each of the three linked rings. **a** Circulation in ring 1 over time drops in value as the ring weakens. Linking results in higher circulation values at 139° and 180°. **b** Circulation at slices through ring 2. The slice at $\theta = 0°$ follows the trend seen in ring 1 at 180° due to linking. The circulation at $\theta = 139°$ increases as ring 3 is shed. **c** Circulation over time for ring 3. Only times during and after the shedding of the third ring are shown for clarity. The slice at 319° is closest to the location of linking with ring 2. Circulation at 180° increases and as the upper half of the ring is shed last.

Table 4.4: Circulation and impulse at the time of release of each of the linked vortex rings.

Ring	Plane	t (s)	D (cm)	Γ (cm^2/s)	I (gcm/s)
1	90° & 270°	0.000	1.98	4.55	14.00
2	40° & 220°	0.133	1.75	2.50	6.01
2	90° & 270°	0.133	1.77	2.38	5.85
3	40° & 220°	0.267	1.80	2.34	5.95

Since circulation clearly increases as the ring is shed and then rapidly decays, fluid impulse is calculated at the time closest to the release of the ring. To avoid the effects of linking, calculations use the circulation and diameter in the planes perpendicular to the location of linking in the cores. In the second ring, impulse is calculated in two planes, perpendicular to the locations of linking with both the first and third rings, and shows good agreement across both locations. The first ring shed is clearly the strongest with I = 14.00 gcm/s, with the subsequent two much closer in strength at roughly 6 gcm/s. However, due to the limited field of view, analysis of body kinematics leading up to the release of this stronger ring was not possible.

4.2 Turning

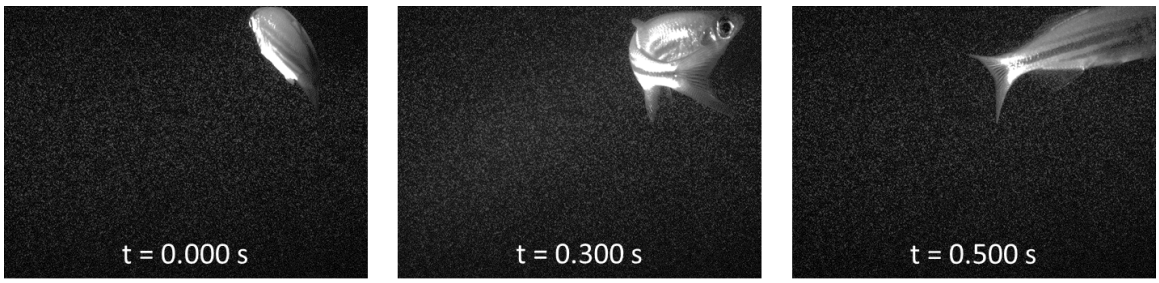

Figure 4-9: Survey images from the center camera during the initialization, execution, and completion of the turning maneuver studied. Contrast has been enhanced for clarity.

One of the most advantageous aspects of fish locomotion is maneuverability; the fish has a natural ability to make fast turns within only small amounts of space. Results are presented here for a 75° turn executed over 0.600 s. Survey images of the

turn at three timesteps can be seen in fig. 4-9.

As the fish initiates the turn, vorticity begins to form along the body, before being shed at the caudal peduncle (fig. 4-10). At the same time, a jet can be seen below the body as the fish turns through the volume. For the following reported results, t = 0.000 s corresponds to the frame in which the fish initializes the turn. Much of the wake analysis is conducted after the fish has completed the turn and resumed forward swimming in its new orientation at t = 0.600 s.

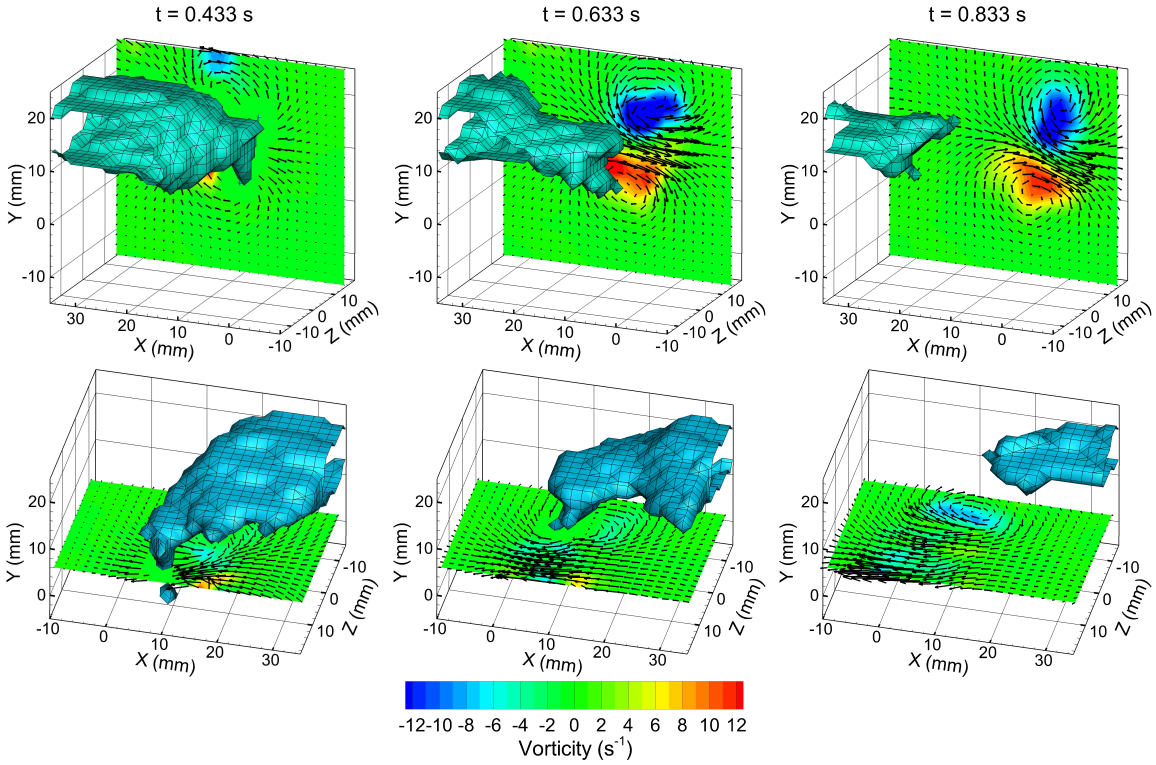

Figure 4-10: Wake during turn execution and after completion as visualized using SAPIV during a 75° turn executed over 0.600 s. The turn was initialized at t = 0.000 s. Simultaneous slices through the caudal fin and below the fish body show the vorticity forming along the body and the thrust jet left behind in the wake. The time t = 0.833 s is the first instance in which the vortex loop is observed to close on itself instead of on the fish body.

At t = 0.833 s, the vortex ring in the wake closes on itself instead of on the fish body for the first time. The resultant vortex loop (fig. 4-11) has substantially higher circulation than either forward swimming case. The shape of the isovorticity contour is more elliptical than during forward swimming, in which the ring is virtually

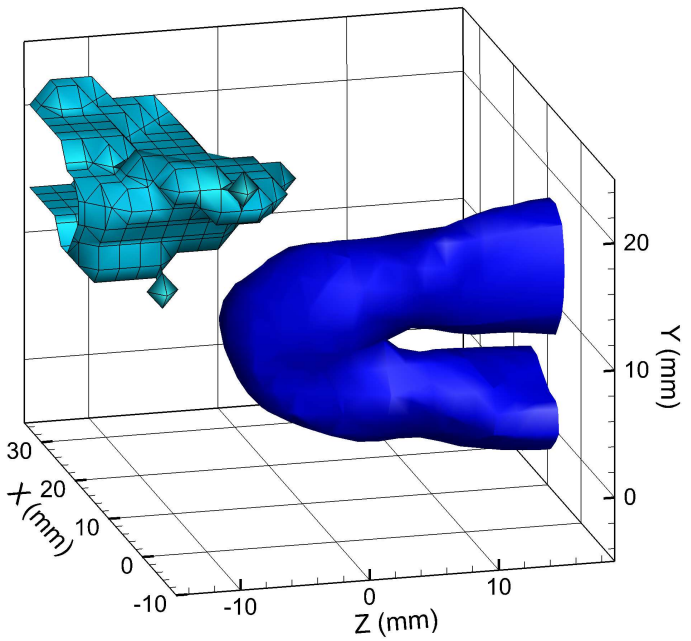

Figure 4-11: Closure of the vortex loop on itself after release by the fish during a 75° turn. The isovorticity contour is drawn at 8 s^{-1}. The vortex loop extends beyond the measurement volume in the +Z direction, preventing complete determination of the wake geometry.

axisymmetric. The mean ring diameter over time in the X-Y plane is D = 1.79 cm, close to that observed in the linked rings during forward swimming at 1.38 L/s. However, the diameter in the X-Z plane is in excess of 2.00 cm, with complete limits extending beyond the measurement volume. Most of the ring's width is occupied by the center thrust jet, not the vortex cores, which have a mean diameter in the X-Y plane of D_0 = 1.10 cm and in the X-Z plane of D_0 = 0.95 cm.

Circulation and ring diameter are calculated in the X-Y plane at eight timesteps from t = 0.567 s to t = 1.033 s (fig. 4-12). Since a center could not be determined from the partial loop, the slice plane used for impulse is located at Z = 11.0 mm. This plane is the location of the peak values of X-Y vorticity at t = 0.000 s. The ring diameter is slightly larger than the mean diameter measured during forward swimming at 1.00 L/s, but consistent with those observed at 1.38 L/s. The vortex core diameter varied substantially, but generally fell within the same limits observed during forward swimming as well.

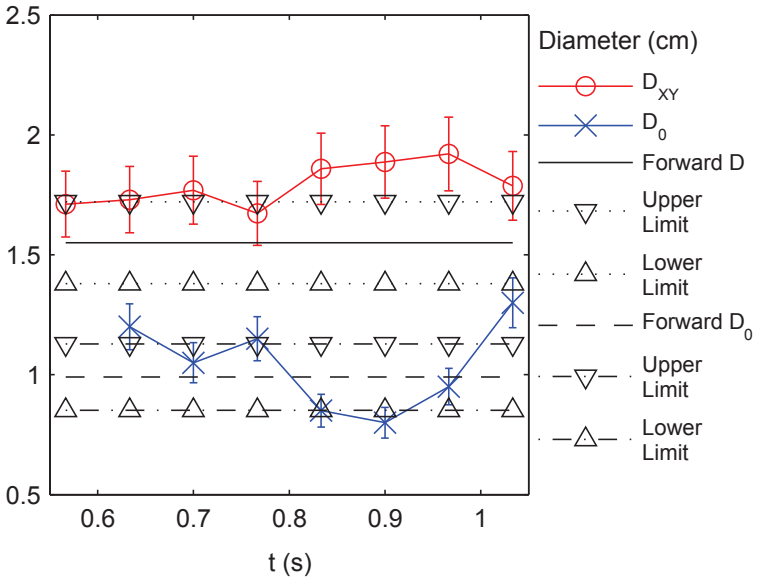

Figure 4-12: Vortex ring diameter and core diameter during turning. The ring diameter is measured over time from t = 0.567 s to t = 1.033 s. The vortex ring is still attached to the fish at t = 0.567 s, prohibiting calculation of core diameter without interference from the body. Core diameter is measured beginning at t = 0.633 s. The mean values and range for the single forward swimming ring (one timestep) is also presented for comparison.

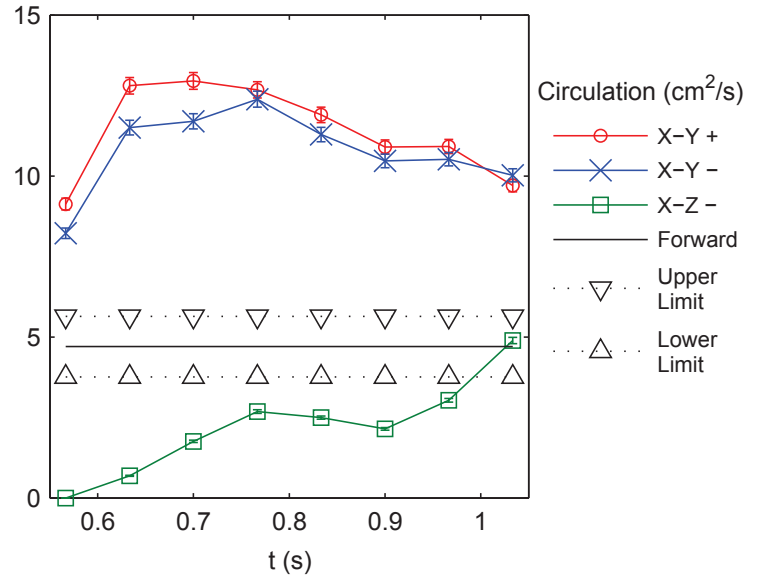

Figure 4-13: Circulation magnitude in the X-Y plane and half of the X-Z plane over time. The circulation values in the X-Y plane peak at t = 0.700 s and then begin to fade. Circulation in the X-Z plane is lower in magnitude and appears to still be rising even as circulation in the X-Y plane drops at t = 0.900 s and later.

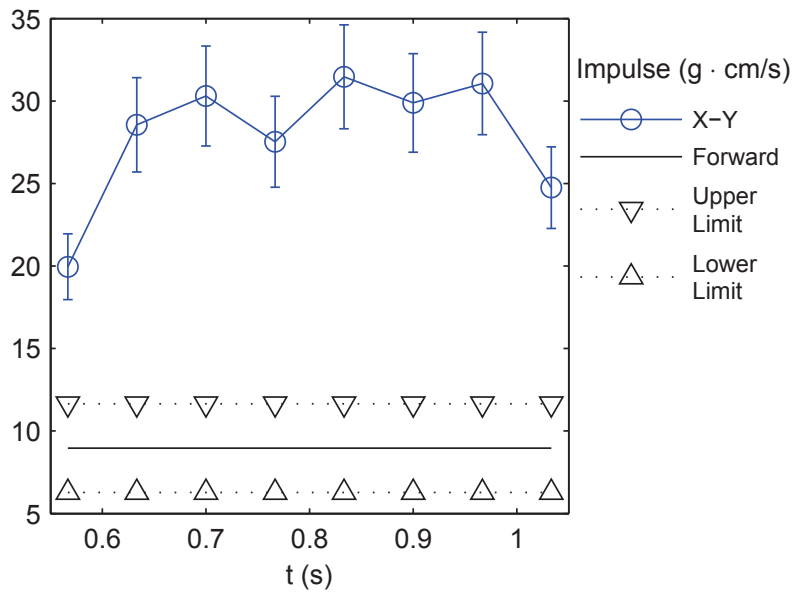

Figure 4-14: Impulse calculated over time in the X-Y plane. The turning impulse is much stronger than during low-speed forward swimming.

The circulation in the two vortex cores measured on the X-Y plane shows good agreement in magnitude and peaks as the ring is shed from the body (fig. 4-13). The circulation in the X-Z plane grows as the loop is released from the fish body, but has not matched the strength measured in the X-Y plane, even as the X-Y slices have begun to decay substantially.

The impulse at each time is also analyzed for comparison with forward swimming (fig. 4-14). The impulse increases with circulation, and shows noticeable decline at t = 1.033 s when the circulation has also dropped substantially. Variations in the measured diameter created variation in the calculated impulse, but the results are notably higher than during forward swimming with a peak value of I = 31.46 gcm/s, over twice the maximum impulse observed during forward swimming (I = 14.00 gcm/s in ring 1 at U = 1.38 L/s). The impulse measured during this turn is still much lower than the 91 gcm/s reported by Epps and Techet [18] during a C-start performed by a longer fish at a much faster speed.

Chapter 5

Conclusions and Future Work

Overall, the development of 3D PIV techniques marks a new era for the analysis of swimming hydrodynamics. In this thesis, synthetic aperture PIV has been proven as viable method of reconstructing wake features behind a swimming fish. Through the use of automatic masking to track the fish in arbitrary positions in the measurement volume and a rapid reconstruction algorithm for the particle fields, the technique developed is scalable to the larger amount of data generated by high-speed imaging (with acquisition rates up to 500 Hz). Thus, SAPIV is a promising technique for the analysis of jumping and rapid maneuvering where higher time resolution is necessary. High-speed imaging can also be used to further explore the process by which vortex rings link and the energy balance between the fish and the wake in these scenarios. Additional potential lies in the ability to reconstruct both the body kinematics and the flow field of the fish simultaneously.

Once volumetric PIV fields have been generated, it is possible to expand conventional planar PIV analysis methods for fish wakes, such as the calculation of circulation and impulse, to utilize the additional information that 3D PIV provides. These techniques can be applied over multiple slices through the ring to characterize the geometry and symmetry of these volumetric features. These measurements support the conclusion that an axisymmetric vortex ring model is appropriate for analyzing the dynamics of fish wakes during forward swimming. However, deviations from this shape, including ring linking and more complex vorticity contours, may introduce

errors in analysis from using this assumption at high swimming speeds and during turning maneuvers.

3D PIV measurements also provide a sense of the uncertainty created by 2D PIV analysis of the wake dynamics at what amounts to arbitrary slice locations through the vortex ring. In highly asymmetric behaviors, such as turning, a planar slice cannot fully characterize the wake geometry. Further potential for volumetric PIV exists in generating analysis models that exploit this three-dimensional data, such as direct integration of impulse along contours of arbitrary shape.

In the remainder of this section, specific further developments pertaining to both the implementation and analysis of are discussed.

5.1 High Speed Camera Array

A high-speed camera array has been developed for time-resolved SAPIV experiments. The high-speed array consists of nine Miro 310 cameras from Vision Research capable of running at up to 3200 frames/sec. A preliminary assembly of the high-speed array can be seen in fig. 5-1.

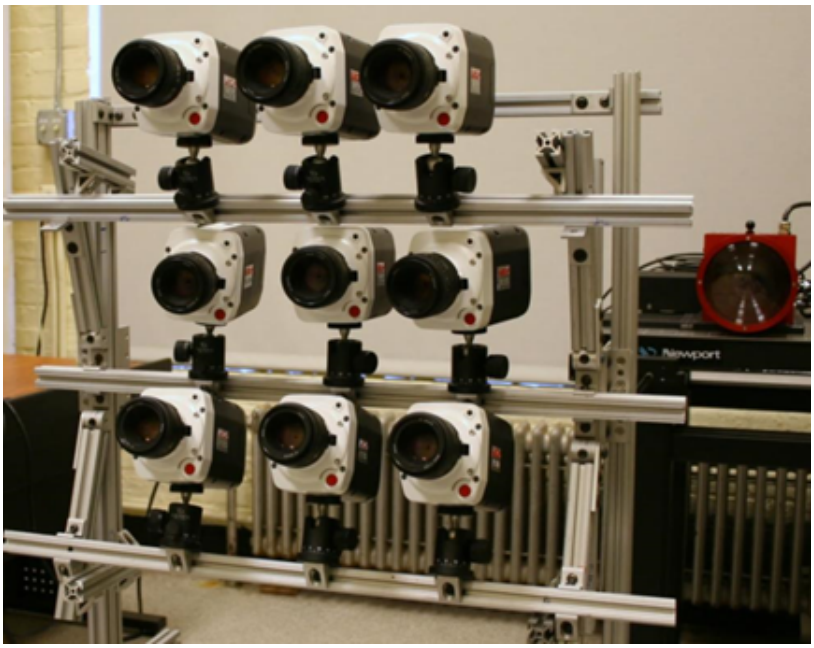

Figure 5-1: High speed camera array for use with new SAPIV experiments

Given the limited Z-resolution of a SAPIV setup, which will always be some fraction of the X-Y resolution of each individual camera, high-speed imaging introduces new options for the processing of SAPIV data. X-Y data can be determined at higher spatial resolutions by using closer images in time, while the sufficient displacement for Z measurement can be found at a higher time interval.

High-speed imaging and improvements to the camera array setup to create a wider field of view will also enable 3D tracking of the fish body over long sequences of time. This will provide more accurate measurement of the Strouhal number and the amount of variation between tailbeats. In addition, reconstructions of the body can be compared to the wake effects that they generate in detail.

5.2 SAPIV Development

As a relatively-new 3D PIV technique, further characterization of SAPIV measurements and the development of new processing codes and filters suitable for this technique are necessary to improve its accuracy and ease of implementation.

The validation analysis performed using a vortex piston provides overall error bounds for measurement of diameter, circulation, and impulse. However, this metric does not separate how much error is due to each stage of the process. To develop more sophisticated methods of quantitative data analysis for 3D PIV, it is desirable to segment uncertainty into errors created during reconstruction and PIV processing and errors generated in the analysis of volumetric PIV data (e.g. in extraction of vorticity).

For the case of a synthetic vortex ring, Belden et al. [9] reports 2% reconstruction error and and 5-10% processing error using MatPIV. Thus, the overall error due to reconstruction and cross-correlation is approximately 12%. However, the error in peak circulation for the validation experiment performed in this study was only 2%. This suggests that the postprocessing filters applied to the data are effective and that the raw measurement errors are small compared to the scale of the actual quantity of interest.

An alternate error analysis method for 3D PIV data utilizes conservation of mass within incompressible fluid flows. Aside from the boundaries of the measurement volume, where outflow must be considered, the velocity field at each voxel in the majority of the volume must satisfy

$$\nabla \cdot u = 0. \tag{5.1}$$

With volumetric data, the divergence of a velocity field can be evaluated numerically using a centered-difference approximation. As demonstrated by Scarano and Poelma [57], the overall error bounds in a voxel can be related to how far the divergence in that voxel is from satisfying continuity. Furthermore, forcing vector fields to satisfy the continuity equation can be used as a filtering technique for error correction [59].

Particle volumes generated by synthetic aperture refocusing can also be processed using particle tracking velocimetry (PTV) [6]. PTV algorithms resolve the velocity of each individual particle and can be used to provide a Lagrangian description of the wake instead of an Eulerian one, an advantage in certain measurement scenarios. The velocity resolution in PIV measurements is limited by the size of the interrogation window. Cross-correlation can also be biased if there is insufficient seeding within each interrogation window. In cases where a large depth in Z is illuminated, the image density (particles/pixel) can be high, while the volumetric seeding density (particles/mm^3) is too low to fill small interrogation windows for PIV. In sparse seeding scenarios and cases where spatial gradients within interrogation windows exist, SAPTV codes can provide higher resolution.

5.3 Further Applications

The 3D velocimetry system developed in this thesis can be applied to numerous additional scenarios in swimming hydrodynamics. Archer fish (genus *Toxotes*) have been widely studied for their ability to spit jets of water accurately at prey through a refractive interface [70]. However, the archer's unique refractive vision also plays

a role in another hydrodynamically-advantageous behavior. The archer fish is also capable of jumping up to two times its body length to capture its prey after stopping below the surface to sight its target. Kinematic analysis by Shih [60] shows that all the thrust production for the jump happens while the fish body is submerged. However, Shih's 2D PIV study of this jumping behavior leaves several ambiguities. The resolved wake is asymmetric, and it is unclear how propulsive vortex rings are structured in 3D. From a single viewpoint, it is also difficult to identify where on the body secondary vortices are forming. The role of smaller fins is important to identify before attempting biomimetic design based on the archer fish's jumping behavior. Since repeatability with live animals is limited, PIV studies in the dorsal plane cannot be easily correlated with studies run on a different jump in the transverse plane.

Another potential application for similar 3D imaging principles is the locomotion of much larger fish. The bluefin tuna is known for its ability to swim at sustained high speeds [12] with remarkable propulsive efficiency. Researchers at the Tuna Research and Conservation Center have trained bluefin tuna to swim in a controlled flume (fig. 5-2), enabling hydrodynamic analysis to be performed on a live swimming tuna.

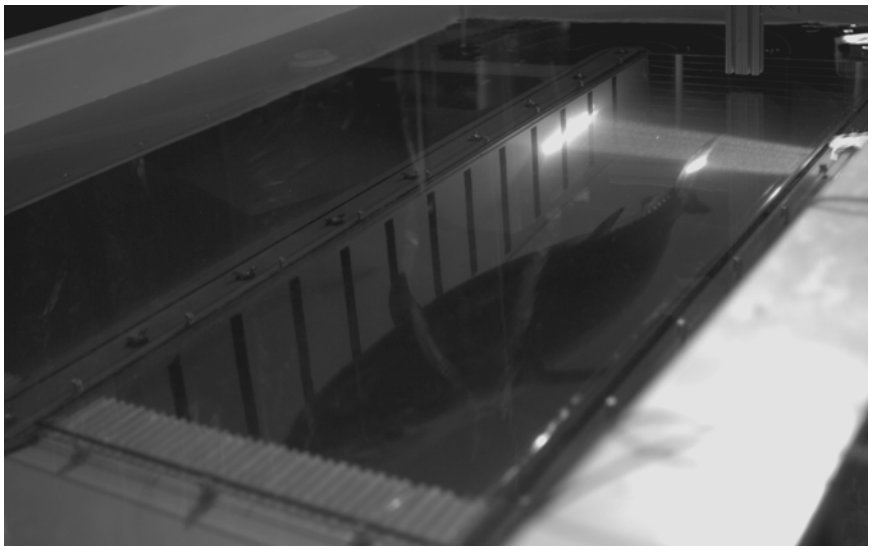

Figure 5-2: Bluefin tuna swimming in the flume at the Tuna Research and Conservation Center during 2D PIV experiments.

Preliminary 2D PIV data taken on the wake of a bluefin tuna revealed that the velocity field observed did not directly follow the motion of the caudal fin in that plane.

Furthermore, unsteadiness exhibited by the tuna while swimming in the flume contributes to the three-dimensional disturbances in the wake. The amount of ambiguity present in 2D measurements proves the need for 3D PIV in this application.

5.4 Hydrodynamic Analysis

In addition to broad applicability, volumetric PIV measurements enable evaluation of more information about the flow field. In this thesis, conventional planar methods for wake analysis were applied over multiple slices through the volume. The impulse calculation in this study only considered the momentum of a vortex ring moving steadily. However, for a toroidal vortex ring, there is also impulse associated with the vortex core:

$$I_1 = \rho\Gamma\frac{\pi D^2}{4}\left[\frac{3}{4}\frac{D_0^2}{D^2}\right]. \tag{5.2}$$

This contribution to the total impulse is substantially less than that of the ring itself, but not nonexistent. When Epps and Techet [18] analyzed the value of I_1 for Giant Danio maneuvering, the computed values were no more than 14% the total value of the total ring impulse. In the validation vortex ring study, the vortex core diameters measured varied by 18%. However, with finer resolution, the core diameter could be determined with more accuracy. This measurement would enable the calculation of this impulse contribution as well.

An even more accurate impulse measurement could be determined through direct integration of the impulse around three-dimensional vorticity contours:

$$I = \frac{1}{2}\rho\int_V \mathbf{x}\times\omega dV. \tag{5.3}$$

To identify the regions of a flow that must be included within these integration contours, 3D PIV data can also be used for direct calculation of vortex identification criteria. For instance, vortex cores can be identified as regions with peak values of the Q-criterion, defined as

$$Q = \frac{1}{2}(|\Omega|^2 + |S|^2), \tag{5.4}$$

where Ω and S are the decomposition of the velocity gradient tensor into symmetric and skew components. In regions where spatial gradients may create a false peak, the vortex cores can be also be identified as the geometric centroids of regions above a Q-criterion threshold [72]. Numerical 3D integration of impulse from 3D PIV data would provide a truer measure of impulse even in cases like turning where the vortex contour is not a symmetric ring.

Bibliography

[1] D. Adhikari and E.K. Longmire. Visual hull method for tomographic PIV measurement of flow around moving objects. *Experiments in Fluids*, 53(4):943–964, 2012.

[2] D. Adhikari and E.K. Longmire. Infrared tomographic PIV and 3D motion tracking system applied to aquatic predatorprey interaction. *Measurement Science and Technology*, 24(2):024011, 2013.

[3] R.J. Adrian. Twenty years of particle image velocimetry. *Experiments in Fluids*, 39(2):159–169, 2005.

[4] J.M. Anderson. *Vorticity Control for Efficient Propulsion*. Phd thesis, Massachusetts Institute of Technology, 1996.

[5] C. Atkinson and J. Soria. An efficient simultaneous reconstruction technique for tomographic particle image velocimetry. *Experiments in Fluids*, 47:553–568, 2009.

[6] A. Bajpayee and A.H. Techet. 3D particle tracking velocimetry (PTV) using high speed light field imaging. In *10th International Symposium on Particle Image Velocimetry*, 2013.

[7] D.S. Barrett, M.S. Triantafyllou, D.K.P. Yue, M.A. Grosenbaugh, and M.J. Wolfgang. Drag reduction in fish-like locomotion. *Journal of Fluid Mechanics*, 392(1):183–212, 1999.

[8] J. Belden. Calibration of multi-camera systems with refractive interfaces. *Experiments in Fluids*, 54(2):1463, 2013.

[9] J. Belden, T.T. Truscott, M.C. Axiak, and A.H. Techet. Three-dimensional synthetic aperture particle image velocimetry. *Measurement Science and Technology*, 21(12):125403, 2010.

[10] J. Buck, G. Cavalcanti, P. Mandel, E. Schumacher, and S.B. Shiplett. Ghost swimmer, a biometric robot fish. 2009 SCOPE Projects, Franklin W. Olin College of Engineering, 2009.

[11] J.O. Dabiri. On the estimation of swimming and flying forces from wake measurements. *Journal of Experimental Biology*, 208(18):3519–32, 2005.

[12] H. Dewar and J.B. Graham. Studies of tropical tuna swimming performance in a large water tunnel - III. Kinematics. *Journal of Experimental Biology*, 192:45–59, 1994.

[13] S. Discetti and T. Astarita. A fast multi-resolution approach to tomographic piv. *Experiments in Fluids*, 52:765–777, 2012.

[14] P. Domenici and R.W. Blake. The kinematics and performance of fish fast-start swimming. *Journal of Experimental Biology*, 200:1165–1178, 1997.

[15] E.G. Drucker and G.V. Lauder. Locomotor forces on a swimming fish: three-dimensional vortex wake dynamics quantified using digital particle image velocimetry. *Journal of Experimental Biology*, 202(18):2393–2412, 1999.

[16] K. D. Ellenrieder and S. Pothos. PIV measurements of the asymmetric wake of a two dimensional heaving hydrofoil. *Experiments in Fluids*, 44(5):733–745, 2007.

[17] G.E. Elsinga, F. Scarano, B. Wieneke, and B.W. van Oudheusden. Tomographic particle image velocimetry. *Experiments in Fluids*, 41(6):933–947, 2006.

[18] B.P. Epps and A.H. Techet. Impulse generated during unsteady maneuvering of swimming fish. *Experiments in Fluids*, 43(5):691–700, 2007.

[19] B.P. Epps, P. Valdivia y Alvarado, K. Youcef-Toumi, and A.H. Techet. Swimming performance of a biomimetic compliant fish-like robot. *Experiments in Fluids*, 47(6):927–939, 2009.

[20] F.E. Fish, G.V. Lauder, R. Mittal, A.H. Techet, M.S. Triantafyllou, J.A. Walker, and P.W. Webb. Conceptual design for the construction of a biorobotic auv based on biological hydrodynamics. In *International Symposium on Unmanned Untethered Submersible Technology*, 2003.

[21] B.E. Flammang, G. V. Lauder, D. R. Troolin, and T. Strand. Volumetric imaging of shark tail hydrodynamics reveals a three-dimensional dual-ring vortex wake structure. *Proc R Soc B*, 278(1725):3670–3678, 2011.

[22] B.E. Flammang, G.V. Lauder, D.R. Troolin, and T.E. Strand. Volumetric imaging of fish locomotion. *Biology letters*, 7(5):695–698, 2011.

[23] Blender Foundation. Blender 3D Creation Software. http://www.blender.org, 2013.

[24] A. Gao and A.H. Techet. Design considerations for a robotic flying fish. In *OCEANS 2011*, 2011.

[25] S. Ghaemi and F. Scarano. Multi-pass light amplification for tomographic particle image velocimetry applications. *Measurement Science and Technology*, 21(12):127002, 2010.

[26] Raytrix GmbH. Raytrix 3d light field camera technology. http://www.raytrix.de, 2013.

[27] J. Gray. Studies in animal locomotion I. the movement of fish with special reference to the eel. *Journal of Experimental Biology*, 10:88–104, 1933.

[28] R. Hain, C.J. Kähler, and D. Michaelis. Tomographic and time resolved PIV measurements on a finite cylinder mounted on a flat plate. *Experiments in Fluids*, 45(4):715–724, 2008.

[29] G.M. Hale and M.R. Querry. Optical constants of water in the 200-nm to 200-μm wavelength region. *Applied Optics*, 12(3):555–563, 1973.

[30] R. Hartley and A. Zisserman. *Multiple View Geometry in Computer Vision*. Cambridge University Press, 2000.

[31] K.D. Hinsch. Holographic particle image velocimetry. *Measurement Science and Technology*, 13:R61–R72, 2002.

[32] A. Isaksen, L. McMillan, and S.J. Gortler. Dynamically reparameterized light fields. In *Proceedings of the 27th annual conference on Computer graphics and interactive techniques - SIGGRAPH '00*, pages 297–306, New York, New York, USA, 2000. ACM Press.

[33] Y.J. Jeon and H.J. Sung. Three-dimensional PIV measurement of flow around an arbitrarily moving body. *Experiments in Fluids*, 53(4):1057–1071, 2012.

[34] A. Kassir and T. Peynot. Reliable automatic camera-laser calibration. In *Australasian Conference on Robotics and Automation*, 2010.

[35] R.D. Keane and R.J. Adrian. Theory of cross-correlation analysis of PIV images. *Applied scientific research*, 49(3):191–215, 1992.

[36] D. Kim and M. Gharib. Characteristics of vortex formation and thrust performance in drag-based paddling propulsion. *Journal of Experimental Biology*, 214:2283–2291, 2011.

[37] J. Kitzhofer, T. Nonn, and C. Brücker. Generation and visualization of volumetric piv data fields. *Experiments in Fluids*, 51:1471–1492, 2011.

[38] R.R. La Foy and P. Vlachos. Analysis of an optimized mlos tomographic reconstruction algorithm and comparison to the mart reconstruction algorithm. In *64th annual meeting of the APS division of fluid dynamics*, 2011.

[39] G.V. Lauder. Swimming hydrodynamics: ten questions and the technical approaches needed to resolve them. *Experiments in Fluids*, 51(1):23–35, 2009.

[40] G.V. Lauder and P.G. Madden. Advances in comparative physiology from high-speed imaging of animal and fluid motion. *Annual review of physiology*, 70:143–163, 2008.

[41] G.V. Lauder and P.G.A. Madden. Learning from fish: Kinematics and experimental hydrodynamics for roboticists. *International Journal of Automation and Computing*, 3(4):325–335, 2006.

[42] M. Levoy. Light fields and computational imaging. *Computer*, 39:46–55, 2006.

[43] J.C. Liao, D.N. Beal, G.V. Lauder, and M.S. Triantafyllou. Fish exploiting vortices decrease muscle activity. *Science*, 302(5650):1566–9, 2003.

[44] J. Lighthill. *Mathematical Biofluiddynamics*. Society for Industrial and Applied Mathematics, 1975.

[45] J.D. Luff, T. Drouillard, A.M. Rompage, M.A. Linne, and J.R. Hertzberg. Experimental uncertainties associated with particle image velocimetry (PIV) based vorticity algorithms. *Experiments in Fluids*, 26:36–54, 1999.

[46] K. Lynch. *Development of a 3-D Fluid Velocimetry Technique based on Light Field Imaging*. Masters thesis, Auburn University, 2011.

[47] D.W. McCutchen. Froude propulsive efficiency of a small fish, measured by wake visualization. In T. Pedley, editor, *Scale effects in animal locomotion*, chapter 22, pages 339–363. Academic, 1977.

[48] H. Meng, G. Pan, Y. Pu, and S.H. Woodward. Holographic particle image velocimetry: from film to digital recording. *Measurement Science and Technology*, 15:673–685, 2004.

[49] U. Muller, B. Heuvel, E. Stamhuis, and J. Videler. Fish foot prints: morphology and energetics of the wake behind a continuously swimming mullet (Chelon labrosus Risso). *Journal of Experimental Biology*, 200(22):2893–906, 1997.

[50] D.W. Murphy, D.R. Webster, and J. Yen. A high-speed tomographic PIV system for measuring zooplanktonic flow. *Limnology and Oceanography: Methods*, 10:1096–1112, 2012.

[51] M. Novara, K.J. Batenburg, and F. Scarano. Motion tracking-enhanced MART for tomographic PIV. *Measurement Science and Technology*, 21:035401, 2010.

[52] F. Pereira, M. Gharib, D. Dabiri, and D. Modarress. Defocusing digital particle image velocimetry: a 3-component 3-dimensional DPIV measurement technique. Application to bubbly flows. *Experiments in Fluids*, 29:S78–S84, 2000.

[53] A.K. Prasad. Stereoscopic particle image velocimetry. *Experiments in Fluids*, 29:103–116, 2000.

[54] M.W. Rosen. Water flow about a swimming fish. No. TP-2298. Naval Ordnance Test Station, China Lake, CA, 1959.

[55] J. Sakakibara, M. Nakagawa, and M. Yoshida. Stereo-PIV study of flow around a maneuvering fish. *Experiments in Fluids*, 36(2):282–293, 2004.

[56] F. Scarano. Tomographic PIV: principles and practice. *Measurement Science and Technology*, 24(1):012001, 2013.

[57] F. Scarano and C. Poelma. Three-dimensional vorticity patterns of cylinder wakes. *Experiments in Fluids*, 47:69–83, 2009.

[58] B.E. Scharfman, D.P. Hart, and A.H. Techet. Light field imaging of turbulent liquid sheet breakup in air. In *10th International Symposium on Particle Image Velocimetry*, 2013.

[59] D. Schiavazzi, F. Coletti, G. Iaccarino, and J.K. Eaton. A matching pursuit approach to solenoidal filtering of three-dimensional velocity measurements. In *10th International Symposium on Particle Image Velocimetry*, 2013.

[60] A.M. Shih. *Hydrodynamics of jumping in archer fish, Toxotes microlepis*. Masters thesis, Massachusetts Institute of Technology, 2010.

[61] M.H.K. Siddiqui. Velocity measurements around a freely swimming fish using PIV. *Measurement Science and Technology*, 18(1):96–105, 2007.

[62] G.R. Spedding, J.M.V. Rayner, and C.J. Pennycuick. Momentum and energy in the wake of a pigeon (*Columba livia*) in slow flight. *Journal of experimental biology*, 111(1):81–102, 1984.

[63] E. Stamhuis and J. Videler. Quantitative flow analysis around aquatic animals using laser sheet particle image velocimetry. *Journal of Experimental Biology*, 198:283–94, 1995.

[64] E.J. Stamhuis, J.J. Videler, L.A. van Duren, and U.K. Muller. Applying digital particle image velocimetry to animal-generated flows: Traps, hurdles and cures in mapping steady and unsteady flows in Re regimes between 10^-2 and 10^5. *Experiments in Fluids*, 33(6):801–813, 2002.

[65] J.K. Sveen. An introduction to matpiv v.1.6.1. eprint no. 2, ISSN 0809-4403, Dept. of Mathematics, University of Oslo, 2004. http://www.math.uio.no/~jks/matpiv.

[66] B.S. Thurow and T. Fahringer. Recent Development of Volumetric PIV with a Plenoptic Camera. In *10th International Symposium on Particle Image Velocimetry*, 2013.

[67] M.S. Triantafyllou, G.S. Triantafyllou, and D.K.P. Yue. Hydrodynamics of Fish-like Swimming. *Annual Review of Fluid Mechanics*, 32(1):33–53, 2000.

[68] E.D. Tytell. Median fin function in bluegill sunfish Lepomis macrochirus: streamwise vortex structure during steady swimming. *Journal of Experimental Biology*, 209(8):1516–1534, 2006.

[69] E.D. Tytell, E.M. Standen, and G.V. Lauder. Escaping Flatland: three-dimensional kinematics and hydrodynamics of median fins in fishes. *Journal of Experimental Biology*, 211(2):187–195, 2008.

[70] A. Vailati, L. Zinnato, and R. Cerbino. How archer fish achieve a powerful impact: Hydrodynamic instability of a pulsed jet in toxotes jaculatrix. *PLoS ONE*, 7(10):e47867, 2012.

[71] V. Vaish, M. Levoy, R. Szeliski, and C.L. Zitnick. Reconstructing Occluded Surfaces Using Synthetic Apertures: Stereo, Focus and Robust Measures. In *2006 IEEE Computer Society Conference on Computer Vision and Pattern Recognition - Volume 2 (CVPR'06)*, volume 2, pages 2331–2338. Ieee, 2006.

[72] B.G. van der Wall and H. Richard. Analysis methodology for 3c-piv data of rotary wing vorticles. *Experiments in Fluids*, 40:798–812, 2006.

[73] J.J. Videler. *Fish Swimming*. Chapman & Hall, 1993.

[74] M.J. Wolfgang, J.M. Anderson, M.A. Grosenbaugh, D.K. Yue, and M.S. Triantafyllou. Near-body flow dynamics in swimming fish. *Journal of Experimental Biology*, 202(17):2303–27, 1999.

[75] Q. Zhu, M.J. Wolfgang, D.K.P. Yue, and M.S. Triantafyllou. Three-dimensional flow structures and vorticity control in fish-like swimming. *Journal of Fluid Mechanics*, 468:1–28, 2002.